Discontinuous segregation patterning across disconnections

Chongze Hu, Stéphane Berbenni, Douglas Medlin, Rémi Dingreville

Graphical Abstract

Discontinuous segregation patterning across disconnections

Chongze Hu, Stéphane Berbenni, Douglas L. Medlin, Rémi Dingreville

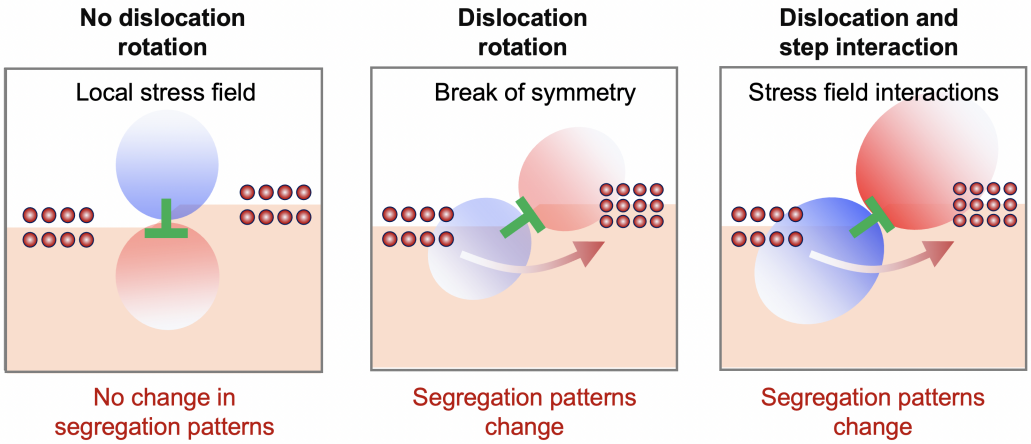

Discontinuous segregation patterning across disconnections

Chongze Hu[a], Stéphane Berbenni[b,c], Douglas L. Medlin[d], Rémi Dingreville[a,*]

[a] *Center for Integrated Nanotechnologies, Sandia National Laboratories, Albuquerque, NM 87185, USA*
[b] *Université de Lorraine, CNRS, Arts et Métiers ParisTech, LEM3, F-57000 Metz, France*
[c] *Laboratory of Excellence on Design of Alloy Metals for Low-mAss Structures (DAMAS), Université de Lorraine, F-57000 Metz, France*
[d] *Sandia National Laboratories, Livermore, CA, 94551, USA*

Abstract

Twinning is a frequent deformation mechanism in nanocrystalline metals, and segregation of solute atoms at twin boundaries is a thermodynamic process that plays an important role in the stability and strengthening of these materials. In pristine, defect-free twin boundaries, solute segregation generally follows a single- or multi-layer patterned coverage of solutes that is uniformly and symmetrically distributed at segregation sites across the boundary. However, when a disconnection, a type of interfacial line defect, is present at the twin boundary, we report a possible discontinuity of the segregation patterns across this defect for a broad range of binary alloys. The change of segregation pattern is explained by a break of the local symmetry across the disconnection terraces. The characteristics of this change are dictated by the orientation of the dislocation content sitting at the step region of the disconnection and its synergistic/antagonistic interactions with the step character. These findings not only advance our understanding of the origin of the interface segregation phenomena and the key contribution from interfacial defects, but they also shed light on applications for tailoring atomically precise interfacial structures to design alloys with emerging properties.

Keywords: Twin boundary, Segregation, Disconnection, Dislocation,

*Corresponding author
Email address: rdingre@sandia.gov (Rémi Dingreville)

1. Introduction

Twin boundaries are special grain boundaries with mirror symmetries and lower interfacial energies than that of general grain boundaries. These characteristics endow twin boundaries with unique properties that play a central role in the thermodynamics, stability, formability, and mechanical properties of nanocrystalline metals [1–3]. Segregation of solute atoms at these boundaries is known to affect many of their attributes, including atomic structure and thermodynamics [4–8], boundary kinetics [9, 10], mechanical [11–13], or electrical properties [14]. The accepted notion is that solute segregation patterns (also called segregation structures or segregation superstructures) at pristine twin and symmetric boundaries follow the classical McLean-type segregation. In this thermodynamic context, solute segregation generally occurs as a single- or multi-layer coverage of solute atoms located at the boundary line or distributed symmetrically across it [15–21]. These segregation patterns can also be affected by atomic-size mismatch between the solvent and solute, where solute atoms larger than solvent atoms would favorably segregate to expanded segregation sites, while smaller solutes would segregate to compressive sites [17, 22–26]. Previous studies primarily investigated these segregation structures in defect-free, ground-state grain boundaries [6, 20, 27–29]. However, such segregation superstructures are not necessarily representative since the majority of boundaries in nanocrystalline materials are not often in their ground state, but rather in a far-from equilibrium. Such non-equilibrium grain boundaries are often accompanied by interfacial line defects [10, 30–32].

When interfacial line defects are present at twin boundaries, they typically separate well-defined coherent terraces. In general, these line defects, which are termed disconnections [10, 30, 31, 33], have both dislocation- (with Burgers vector $\mathbf{b}$) and step-like (with step height h_{step}) characters. Previous analyses in pure metals [31, 34–42] have highlighted the importance of the dislocation core relaxation at the disconnection on the resulting relaxed (defected) boundary structure. For instance, in gold (Au), $1/3\langle 111\rangle$ twin boundary disconnections adopt two distinct relaxed structures: one configuration with a localized core and a second configuration with a dissociated core composed of a stacking fault terminated by a Shockley partial dislocation [37]. The structural difference between the two configurations depends

on the orientation of the Burgers vector **b** with respect to the twin plane, which dictates the pathways available for the defect to relax its core structure. Yet, solute segregation behaviors at these types of defected boundaries, particularly the interplay with the local line defect, have not been studied thoroughly.

In this study, we are interested in the role of these disconnections on solute segregation at twin boundaries. More precisely, we want to understand the role of the step region and dislocation sitting near that step region on solute segregation patterns. To address this question, we employed molecular static simulations, dislocation circuit analysis, and continuum-based fast Fourier transform (FFT) micromechanics calculations of interfacial line defects to investigate solute segregation near pristine and disconnected $\Sigma3(111)$ twin boundaries for twelve different face-centered cubic (FCC)-based binary alloys. We report the possibility of a discontinuity in the segregation patterns across the two twin-boundary terraces composing the disconnection under specific conditions (Fig. 1). We show that for specific boundary configurations the disconnection can break the symmetry of the local stress field and change the segregation pattern from one type to another. We find a discontinuous interfacial segregation behavior for which the segregation patterns can change from segregation to anti-segregation or vice versa regardless of the initial segregation pattern characterizing the reference disconnection-free twin boundary. Characteristics of the change in the segregation pattern are dictated by the character and orientation of the dislocation content of the disconnection, driving changes in the local hydrostatic pressure field and local segregation volume in the vicinity of the boundary. We analyze these characteristics, which are consistently observed across twelve different binary alloys for disconnections of varying step height and dislocation character.

2. Methods

2.1. Atomistic simulations

We performed all of our molecular statics (MD) simulations using the Large-scale Atomic/Molecular Massively Parallel Simulator (LAMMPS) code [43]. In total, we studied twelve A-B binary alloys, namely: Cu–Zr, Cu–Ag, Cu–Ni, Cu–Pt, Cu–Ta, Al–Ga, Al–Mg, Al–Pb, Ni–Zr, Ni–V, Ni–Pd, and Pt–Au. In this A–B alloy notation, the first element A refers to the solvent atom, while the second element B denotes the solute atom. For instance, in Al–Ga, Al is the solvent matrix and Ga is the solute. For each of these twelve binary

alloys, we studied six different twin-boundary/defect structures. First, we constructed the atomistic simulation cell for the pristine reference $\Sigma3(111)$ twin-boundary structure with the $[1\bar{2}1]$, $[111]$, and $[\bar{1}01]$ lattice directions parallel to the x-, y-, and z-axis respectively (Fig. 2a). The entire simulation cell for the pristine twin-boundary configuration has a dimension of $\sim$ 14.6 nm $\times$ 11.0 nm $\times$ 2.8 nm and contains 28800 atoms. Based on this $\Sigma3(111)$ twin-boundary structure, we constructed two disconnection configurations. The first disconnection type was constructed by shifting a half (111) atomic layer in the $\Sigma3(111)$ twin boundary. This construct resulted in a compact, localized dislocation at the disconnection. We refer to this configuration as the "unfaulted disconnection" (or UFD, see Fig. 2b-d). Three different UFD configurations were built, including: (i) one unfaulted disconnection with a Burgers vector, $\mathbf{b} = 1/6[121]$, and a relatively small step height h_{step} (named UFD1, see Fig. 2b), (ii) one unfaulted disconnection with $\mathbf{b} = 0$ and a larger h_{step} (named UFD2, see Fig. 2c), (iii) one unfaulted disconnection with $\mathbf{b} = -1/3[1\bar{1}1]$ and a small h_{step} (named UFD3, Fig. 2c). We also constructed a second disconnection configuration by removing different number of partial (111) atomic layers on one side of the $\Sigma3(111)$ twin boundary, and then relaxing the atomic positions for entire simulation cells via minimization. This construct relaxed to a dissociated configuration, by emitting a Shockley partial dislocation and a trailing stacking fault in the bulk crystal. Here, we refer to this type of disconnection configuration as a "faulted disconnection" (FD, see Fig. 2e-f). We constructed two FD configurations, with a Burgers vector $\mathbf{b} = 1/3[1\bar{1}1]$ and $\mathbf{b} = 1/2[101]$ and two different step heights h_{step} (named as FD1 for smaller h_{step} and FD2 for larger h_{step}, see Fig. 2e-f). Note that in prior studies [37], UFD3 with $\mathbf{b} = -1/3[1\bar{1}1]$ was also referred to as an 'interior' disconnection, while the FD1 with $\mathbf{b} = 1/3[1\bar{1}1]$ was referred to as an 'exterior' disconnection. Their Burgers vectors are flipped by 180° rotation from one another. For all the disconnection configurations listed above, we performed an energy minimization to optimize the atom coordinates and lattice parameters. We applied periodic boundary conditions in all directions. The convergence criteria for energy and forces were set to 10^{-8} and 10^{-10} respectively.

Based on these relaxed disconnection configurations, we calculated the site-specific, grain-boundary segregation energy (E_{seg}) for the solute atom in each binary alloy via:

$$E_{\text{seg}} = E_{\text{twin}}^{\text{solute}} - E_{\text{bulk}}^{\text{solute}}, \tag{1}$$

where $E_{\text{twin}}^{\text{solute}}$ and $E_{\text{bulk}}^{\text{solute}}$ are the energies of the solute atom doped at a twin-boundary and bulk site respectively. Since the pristine $\Sigma3(111)$ twin boundary has a highly symmetric structure, we selected a relatively small region with a dimension of ~ 1.4 nm $\times 2.5$ nm $\times 0.7$ nm near the boundary region to calculate the segregation maps (*i.e.* E_{seg} near the disconnection). For both unfaulted and faulted configurations, given the existence of step and dislocations, we used a larger region than in the pristine configuration to calculate the segregation maps, with dimensions of ~ 6.0 nm $\times 6.0$ nm $\times$ 0.7 nm near the disconnections. In total, the number of atomic sites in these selected regions ranged from $\sim$1000 to 1500 depending on the configuration of the specific boundary studied.

2.2. Selection of interatomic potentials

In order to describe the twelve binary-alloy systems studied in this work, we selected interatomic potentials based on availability and relevant data used to fit these potentials (*i.e.* segregation energy, stable/unstable stacking fault energy, elastic constants, grain-boundary energy). Specifically, we used the embedded atom metal (EAM) potentials for Al–Pb [44], Al–Mg [45], Al–Ga [46], Cu–Ni [47], Cu–Zr [48], Cu–Ag [49], Ni–Pd [50], Ni–Zr [51], and Pt–Au [52] binary alloys. We used modified EAM (also called MEAM) potentials for Cu–Pt [53], Ni–Pt [53], and Ni–V [54] binary alloys. Finally, we used an angular dependent potential (ADP) for the Cu–Ta [55] system. Note that all the interatomic potentials above are available on the NIST Interatomic Potentials Repository website [56].

2.3. Grain-boundary descriptors

In order to characterize the correlations between the segregation behavior and the grain-boundary structure, we defined a selected set of descriptors [42]. Notably, we considered descriptors related to (i) the local atomic structure via the centrosymmetry parameter or CSP [57], and (ii) the local deformation and pressure environment using the total volumetric strain due to the atomic arrangement of the boundary, ϵ_{vol}, the segregation volume, ΔV_{seg}, and the local pressure, ΔP_{tot}. The segregation volume is determined by $\Delta V_{\text{seg}} = V_{\text{twin}} - V_{\text{bulk}}$, where V_{twin} and V_{bulk} are the Voronoi volumes of solute atom located at twin and bulk regions, respectively. The total local pressure stems directly from the stress field of the dislocation arrangement near the disconnection, and is defined as the change in pressure when substituting a solute atom at a twin boundary site and in the bulk respectively

such that $\Delta P_{\text{tot}} = P_{\text{twin}} - P_{\text{bulk}}$. We used the OVITO software to perform structural analysis and visualize all atomistic structures [58].

2.4. Dislocation analysis at disconnections

We performed Burgers vector circuit analyses [30] to study the dislocation character and step heights for the six (pristine/defected) twin-boundary configurations studied in this work. This method constructs a closed-loop path around the disconnection and then transfers this closed path to a reference frame defined by the bicrystallography. The closure failure in the reference frame gives the Burgers vector, $\mathbf{b}$, of dislocations. We divided this closed circuit into two segments: C_λ in the upper (λ) crystal and C_μ in the lower (μ) crystal as shown in Fig. 3 (a). By choosing the interface crossings at crystallographically equivalent locations, these vectors can be ignored, and the Burgers vector, $\mathbf{b}$, in the upper λ frame, is then given by:

$$\mathbf{b} = -(\mathbf{C}_\lambda + \mathbf{P}\mathbf{C}_\mu), \tag{2}$$

where $\mathbf{P}$ transforms crystal vectors from the μ to λ crystal coordinate frames, C_λ and C_μ are the circuit paths in the two crystals. The coordinate transformation matrix $\mathbf{P}$ was determined by solving a matrix equation for the unit vectors $\mathbf{t}_\lambda$ and $\mathbf{t}_\mu$ in the two crystal orientations. For our chosen coordinate system $\mathbf{P}$ is given by:

$$\mathbf{P} = \frac{1}{3}\begin{pmatrix} 2 & 2 & -1 \\ -2 & 1 & -2 \\ -1 & 2 & 2 \end{pmatrix}. \tag{3}$$

Equation (2) employs the Finish-Start/Right-Hand (FS/RH) convention (see negative sign in Eq. (2)), with the dislocation line direction defined as positive out of the board. The step heights in the upper and lower crystals were respectively defined as $h_\lambda = \mathbf{C}_\lambda \cdot \mathbf{n}_\lambda$ and $h_\mu = \mathbf{C}_\mu \cdot \mathbf{n}_\mu$, where $\mathbf{n}_\lambda$ and $\mathbf{n}_\mu$ are the interface normals (unit vectors) pointing out of each crystal. The circuit analysis, step heights, and Burgers vectors for all five disconnections in Pt are shown in Fig. 3 and in the Suppl. Fig. S3 in the Supplementary Material. For all disconnection configurations, the circuit analysis indicates the out-of-plane component of the dislocation always cancels either within the individual circuit elements or after combining the circuits, meaning that the net Burgers vectors in all five cases are pure edge dislocations.

2.5. Micromechanics of interfacial line defects

At the continuum scale, we described a disconnection defect as the combination of dislocation and disclination type defects from the Volterra construct. These constructs were simulated using FFT-based continuum micromechanics of interfacial line defects [59, 60] to numerically compute the normalized hydrostatic stress field (σ_{kk}/E, where E denotes the isotropic Young's modulus) for unfaulted (*i.e.* UFD1 and UFD3) and faulted (*i.e.* FD1) disconnection configurations embedded in an isotropic elastic medium. This method was chosen due to its generalization to model generic boundaries with steps and dislocations since they can be mathematically represented as a set of disclination dipoles and dislocations capturing both short- and long-range elastic fields of such defects [61]. Thus, this method allowed us to resolve elastic strain and curvature effects as seen in our atomistic model using a continuum field approach instead. Since all the FCC-based alloys investigated here always share similar dislocation and step features for the same type of disconnection configuration, we only computed the hydrostatic stress field in the case of platinum-based disconnections as our material model of choice. Here, we used the isotropic elastic constants calculated by our atomistic simulation in Pt [52] with Young's modulus $E = 168$ GPa, a Poisson ratio $\nu = 0.38$, and a lattice constant $a = 0.392$ nm.

From the definitions of $\mathbf{t}_\lambda$ and $\mathbf{t}_\mu$, we described the defect density of the UFD1 configuration (see later Fig. 8 (b) in Results) as a single wedge disclination dipole with length 0.47 nm, since both vectors have same magnitude in this configuration and form a pure rotational discontinuity. Here, the dipole length corresponds to the step height (h_{step}) measured in our atomistic model and dislocation analysis (see Fig. 3 (b)). The angle formed by the step and the x-axis is 90°. The Frank vector magnitude for UFD1 is set to $\omega_z = b/h_{\text{step}}$, where b is the magnitude of $\mathbf{b} = 1/6[121]$. Thus, the disclination dipole is characterized by a non-zero disclination density component $\theta_{zz} = \pm\omega_z t_z/A$ (see later Fig. 8 (a) in Results), where ω_z is the magnitude of the Frank vector (pseudovector), $t_z = 1$ the unit line vector and A is the area spread by the defect core on the numerical grid. Here, the z-axis follows the straight defect line and rotation axis to define the Frank vector component. Compared to a pure single edge dislocation, the advantage to use a disclination-based mechanics is to integrate the step character of the defect in addition to the Burgers vector (see later Fig. 9 in Results).

For the UFD3 and FD1 configurations, the closed loop path around the disconnection needs to consider some combinations of both dislocation and

disclination densities. The edge dislocation in the disconnection and dislocation due to stacking fault (for FD1) are defined by two dislocation density tensors (Nye tensors) containing two non zero components: $\alpha_{xz} = b_x t_z/A$ and $\alpha_{yz} = b_y t_z/A$, where A is the area spread by the dislocation core on the numerical grid, b_x and b_y are projections of the Burgers vector onto the x and y axes, respectively, and $t_z = 1$ is the unit line vector.

For UFD3 and FD1, the dislocation Burgers vector magnitude at the disconnection is given by the difference of magnitudes between vectors $\mathbf{t}_\mu$ and $\mathbf{t}_\lambda$, vectors $\mathbf{t}_\mu$ and $\mathbf{t}_\lambda$, respectively. In the case of the UFD3 configuration (see later Fig. 8 (c) in Results), b_x and b_y are the components of the Burgers vector, which lies on an inclined step forming an angle of 75.255° with the x-axis. This angle is chosen as the average angle formed by $\mathbf{t}_\mu$ (*i.e.* 79.98°) and $\mathbf{t}_\lambda$ (*i.e.* 70.53°). Then, from geometrical considerations, the half-arm of the disclination dipole is 0.17 nm/ $\cos(14.745°)$, where h_{step}=0.17 nm. The magnitude of the Frank vector is given by the angle between $\mathbf{t}_\mu$ and $\mathbf{t}_\lambda$, *i.e.* 9.45°. In the case of the FD1 configuration after dissociation, the dislocation Burgers vector at the disconnection due to the stair-rod dislocation ($\alpha\delta$) is oriented at an angle of 125.6° to the x-axis, then defining its components b_x and b_y. The disconnection step is inclined at an angle of 62.635° to the x-axis (chosen as the average angle formed by $\mathbf{t}_\lambda$ (*i.e.* 70.53°) and $\mathbf{t}_\mu$ (*i.e.* 54.74°). Therefore, the half-arm of the disclination dipole is 0.165 nm/ $\cos(27.365°)$ and the disclination Frank vector magnitude is 15.79° (defined as the angle between angle between $\mathbf{t}_\lambda$ and $\mathbf{t}_\mu$). Additionally, the Shockley partial dislocation ($\boldsymbol{\delta}\mathbf{A}$) is taken from our atomistic simulations and is located at a polar distance from the center of the disconnection of 2.884 nm (length of stacking fault) and at an angle of 70.53° to the x axis. Hence, its Burgers vector is given by $b_x = a\sqrt{6}/6\cos(70.53°)$, $b_y = a\sqrt{6}/6\sin(70.53°)$.

For the five disconnection configurations studied in our atomistic simulation, the dislocation character is fixed and pre-determined by the mismatch of step height at the twin boundaries upon relaxation. However, our FFT-based micromechanics simulations enable us to parametrically change the character of the dislocation and the magnitude of the step height. As discussed in the Results section, we therefore also conducted simulations with various hypothetical dislocation and step configurations to illustrate and isolate their role on the stress field near the disconnection. For all the configurations listed above (atomistic-based or hypothetical), we simulated the normalized hydrostatic stress profiles given by the numerical calculations using our FFT-based dislocation-disclination method [59, 60] and then visualized these profiles us-

ing the Paraview software [62].

3. Results and Discussion

3.1. Crystal structures of Σ3(111) twin-based disconnections

For all twelve binary alloys, we studied six different twin-boundary configurations: the pristine reference Σ3(111) twin boundary and five types of disconnection structures with different step heights and dislocation features, totalling seventy two twin-boundary structures for various combinations of solvent and solute atoms. Details on the construction of these atomic configurations are provided above in the Methods section. We show in Fig. 2 an example of the relaxed atomic structures and corresponding common neighbor analysis (CNA) of the pristine twin boundary and five associated disconnection configurations for Pt. Relaxed disconnection structures for Cu, Ni, and Al are presented in Suppl. Fig. S1 in the Supplementary Material. This display of atomic structures for defected twin boundaries shows that the different pathways available for the defect to relax lead to structural differences that are alike for all the base materials systems studied (*i.e.* for Ni, Cu, Al, and Pt), regardless of the magnitude of the step height.

In agreement with previous studies in Al, Au, Ni, and Pt [36, 37, 42, 52], we observed the multiplicity of structures depending on the type of disconnection and accessible pathways by which its dislocation content could relax. Figures 2 (b-f) illustrate the two classes of disconnected structures: unfaulted and faulted. Panels (b), (c) and (d) show three types of unfaulted structures (UFD1, UFD2, and UFD3) and panels (e) and (f) illustrate two types of faulted structures (FD1 and FD2). The nomenclature of these disconnection configurations can be found in the Methods section.

We adopted the Burgers circuit mapping method to analyze the dislocation characteristics for each disconnection configuration (see Methods for more details). The coordinate frame for circuit analysis is illustrated in Fig. 3 (a). Figures 3 (b-d) show the circuit mapping of three representative configurations in the case of Pt: UFD1, UFD3, and FD1. The corresponding dislocation configurations and steps at these disconnections are displayed in Fig. 3 (e-g). Based on this circuit analysis, we find that UFD1 joins a step of $2d_{111}$ (where d_{111} is the interplanar distance of (111) plane) in the upper crystal λ and with a step of $2d_{111}$ in lower crystal μ (Fig. 3 (b)). Since the step heights are matched, there is no Burgers vector component normal to the interface, but there is a component parallel to the interface equal to 1/6[121]

($\mathbf{D}\alpha$), see (Fig. 3 (a)). This defect is composed of two 30° $1/6 < 112 >$ dislocations, with opposite screw components, on the adjacent $(1\bar{1}1)$ planes (*i.e.* $\boldsymbol{\alpha}\mathbf{B} + \boldsymbol{\alpha}\mathbf{C} = \mathbf{D}\boldsymbol{\alpha}$) [3]. The dislocation analysis for UFD2 also indicates that there is no Burgers vector component normal to the interface because of the matched step heights, see Suppl. Fig. S2 in the Supplementary Material. In contrast to the UFD1 and UFD2 configurations, the step heights for UFD3 (interior disconnection) are mismatched, resulting in Burgers vector components normal to the interface [37]. The step heights for UFD3 are $+1d_{111}$ in λ and $+2d_{111}$ in μ, and the Burgers vector is $-1/3[1\bar{1}1]$ ($\mathbf{A}\boldsymbol{\delta}$), see Fig. 3 (c). Similar to UFD3, FD1 (exterior disconnection) also has mismatched step heights, but its step heights are $+2d_{111}$ in λ and $+1d_{111}$ in μ. The mismatch of step heights also causes FD1 to have Burgers vector components normal to the interface (Fig. 3 (f)). The net Burgers vector in FD1 is $+1/3[1\bar{1}1]$ ($\boldsymbol{\delta}\mathbf{A}$), and this type of defect dissociates by emitting a $1/6[1\bar{2}1]$ ($\boldsymbol{\delta}\mathbf{A}$) dislocation and a stacking fault into the upper crystal, leaving behind a stair-rod dislocation ($\boldsymbol{\alpha}\boldsymbol{\delta}$) at the interface [37, 63] (Fig. 3 (f)). The mismatch of step heights in FD2 configuration also gives a Burgers vector component normal to the interface same as FD1, but the FD2 has larger step heights (see Suppl. Fig. S2 in the Supplementary Material).

3.2. Segregation patterning near pristine twin boundaries

The analysis of the segregation behavior of solute atoms at the pristine, defect-free, reference $\Sigma 3(111)$ twin boundary for the twelve binary alloys reveals a variety of possible segregation superstructures depending on the combination of solvent/solute atoms. In Fig. 4, we show the palette of segregation patterns for all twelve alloys. In this figure, atoms are colored according to their segregation energy, E_{seg}, where the atomic sites with positive E_{seg} (red color) represent unfavorable segregation sites, while atomic sites with negative E_{seg} (blue color) indicate favorable segregation sites (for interpretation of the colors in the figure(s), the reader is referred to the web version of this article.). Here, we adopted the terminology "anti-segregation" and "segregation" to describe the unfavorable and favorable solute segregation at those sites. Note that for each binary system (A–B), the solvent matrix element (A) is always a FCC-based metal (*i.e.* Cu, Ni, Al, and Pt). We calculate the change of segregation energy throughout the entire atomic structure for a given solute type (B).

We report at least three types of segregation patterns for these twelve alloys: a single-layer (1L)-like segregation pattern (Fig. 4 (a)), an alternating

bilayer (2L)-like segregation pattern (Fig. 4 (b)), and a tri- or multi-layer (3L)-like segregation pattern (Fig. 4 (c)). More specifically, four binary alloys, including Al–Ga, Cu–Zr, Al–Mg, and Ni–V, exhibit a single-layer segregation pattern (1L), where the boundary layer of the twin serves as a segregation region (*i.e.* E_{seg} is negative), while the two adjacent atomic planes above and below the boundary plane always exhibit an anti-segregation behavior, see Fig. 4 (a). This class of segregation pattern is coined single-layer because *only* the boundary plane shows a segregation behavior. Note that in the case of Al–Mg, although the adjacent planes two layers away from the boundary plane have negative E_{seg}, their E_{seg} values are much higher than the E_{seg} for the boundary layer. This difference in segregation energies suggests that Mg atoms are highly favorable to segregate at the boundary layer, and thus we still treat Al–Mg as single-layer segregation structure. Meanwhile, four other binary alloys, including Cu–Ag, Cu–Ni, Cu–Pt, and Pt–Au alloys, show an alternating, bilayer segregation pattern (2L), where the twin-boundary plane is, in this case, anti-segregating (*i.e.* E_{seg} is positive at the twin-boundary plane), but the two adjacent atomic planes above and below the boundary plane have a segregating character, see Fig. 4 (c). Finally, the remaining four alloys, *i.e.* Cu–Ta, Al–Pb, Ni–Zr, and Ni–Pd, have a tri- or multi-layer segregation pattern (3L), where all three (or more) boundary layers near the boundary plane have a negative segregation energy, see Fig. 4 (b), and the entire boundary region has a segregating behavior.

3.3. Discontinuous segregation patterning across disconnections

With a clear picture of how solute atoms segregate at defect-free twin boundaries, we now turn our attention to solute segregation at twin boundaries with disconnections. In contrast to the 'quantized'-like segregation patterns observed in the pristine reference boundaries, our analysis of the terraced twin boundaries containing a disconnection shows different segregation behaviors across all five disconnection configurations and alloys. The unfaulted configurations UFD1 and UFD2 (with $\mathbf{b} = 1/6[121]$ for UFD1 and $\mathbf{b} = 0$ for UFD2, *i.e.* pure step) displayed similar segregation behaviors as their pristine twin-boundary counterparts, where both terrace segments show the same segregation patterns as the defect-free twin boundary. In other words, no change occurs in the segregation pattern across the disconnection. However, as shown in Fig. 5, for the disconnection configurations with a Burgers vector not parallel to the boundary plane, *i.e.* for the 'interior' (UFD3), 'exterior' (FD1), and FD2 configurations, we report discontinuous

segregation patterns, where the segregation pattern displayed in the lower terrace is different than the one for the upper terrace. The detailed E_{seg} segregation maps for all configurations and for the twelve binary alloys can be found in Suppl. Figs. S4-S15 in the Supplementary Material. Several key findings can be summarized as follows.

First, in the case of the UFD3 configuration, which exhibits an 'interior' dislocation $\mathbf{b} = -1/3[1\bar{1}1]$, the E_{seg} maps for all twelve binary systems (Figs. 5 (a-c)) show up as a segregation-to-antisegregation change in the segregation patterning (from lower to upper terraces) across the disconnection. Conversely, we can contrast and directly compare the segregation for the UFD3 interior disconnection configuration with that of the FD1 'exterior' counterpart which has its Burgers vector rotated by 180° ($\mathbf{b} = +1/3[1\bar{1}1]$). In the FD1 case, we observe that the E_{seg} maps for all twelve binary systems studied (Figs. 5 (d-f)) show the opposite antisegregation-to-segregation change in the segregation patterning across the disconnection. This observation suggests that the orientation of the dislocation sitting at the step region of the disconnection dictates which terrace has a segregating behavior and which one has an anti-segregating behavior. A similar change in segregation patterning as the one seen in FD1 is also observed for the FD2 configuration (see Suppl. Figs. S4-S15 in the Supplementary Material).

Second, we observe that the change in segregation patterns occurs regardless of the type of initial segregation pattern displayed for the pristine reference twin boundary. Indeed, for the UFD3 configuration, for the alloys systems (Al–Ga, Cu–Zr, Al–Mg, and Ni–V) which presented a single-layer segregation pattern in the pristine case, we observed that the segregation pattern changed from a multi-layer segregating pattern (as seen from the negative E_{seg} atomic layers) for the lower terrace to a multi-layer anti-segregating pattern for the upper terrace (Fig. 5 (a)). The case of Ni–V can be seen as the most extreme case of this change in segregation patterning. Our results show that, for this specific binary system, the disconnection has an accentuating effect on segregation energies in which the upper terrace exhibits a strong anti-segregating behavior and the lower terrace a strong segregating character. Similarly, the four binary systems Cu–Ag, Cu–Ni, Cu–Pt, and Pt–Au display a similar change from a multi-layer segregating pattern for the lower terrace to an anti-segregation behavior on the right-hand side of the disconnection for the upper terrace (Fig. 5 (b)). Likewise, for the remaining four alloys (Cu–Ta, Al–Pb, Ni–Zr, and Ni–Pd), the segregation pattern changes from a trilayer-like segregation for the lower terrace to an anti-segregation

region for the upper terrace. In this case, even though the segregation pattern for the lower terrace remains similar to its pristine, defect-free reference counterpart, it manifests a more segregating character (*i.e* more negative E_{seg} values) compared to the reference case. This trend suggests that the lower terrace promotes segregation even more than in the pristine, defect-free configuration (Fig. 5 (c)).

The results for UFD3, FD1, and FD2 differ from the two unfaulted disconnection configurations UFD1 and UFD2. The analysis of the E_{seg} segregation maps for UFD1 and UFD2 show that there is no difference in segregation behavior between the lower and upper terraces and therefore there is no change in the segregation patterns between the two (see Suppl. Figs. S4-S15 in the Supplementary Material for a comparison amongst all material systems). To illustrate this point more clearly, we extracted the E_{seg} values of the boundary layer for the lower terrace (LT) and upper terrace (UT) regions respectively for the UFD1, UFD3, and FD1 configurations (see Fig. 6 (a)) and then plotted the change of E_{seg} values for some representative binary systems in Figs. 6 (b) and (d). Figure 6 (b) shows the E_{seg} of such boundary layer for the lower and upper terraces for three Cu-based binary systems. The sign of E_{seg} for the lower and upper terraces in UFD1 are always positive, indicating that there is no change in the segregation pattern happening between LT and UT for these three systems. Similarly, in Fig. 6 (d), we plot E_{seg} for the boundary layer for three binary systems which have different segregation superstructures in the pristine reference twin-boundary case. Here again, there is no difference in the sign of E_{seg} between the lower and upper terraces further confirming that the segregation pattern does not change for UFD1. Conversely, in Figs. 6 (b) and (d), we can clearly see that the UFD3 and FD1 configurations respectively displayed a change in the segregation pattern, segregation-to-antisegregation or antisegregation-to-segregation, when going from the lower to upper terrace regions. Overall, we note that this discontinuous change in the segregation pattern is ubiquitous across the various disconnection configurations (*e.g.*, UFD3, FD1, and FD2) and for all twelve binary systems. We further conclude that, given the mirrored behavior between UFD3 and FD1, this discontinuous segregation patterning can be ascribed to the distinct dislocation character of the disconnection.

3.4. Correlation analysis for segregation at disconnections

To identify the origin of this discontinuous segregation patterning, we performed a correlation analysis between E_{seg} and some boundary descrip-

tors. Because prior studies [5, 42] have indicated that the local pressure (ΔP_{tot}) and segregation volume (ΔV_{seg}) have strong correlations with E_{seg}, we only considered these two important boundary parameters in this work (see Methods for the description of boundary descriptors and calculation procedures of ΔP_{tot} and ΔV_{seg}). We also considered other descriptors such as the atomic mismatch between the solvent and solute but those did not reveal any significant correlation and are therefore not presented. By plotting ΔP_{tot} for the lower and upper terraces for all three disconnection configurations (unfaulted, 'interior' UFD3, and 'exterior' FD1) in Figs. 6 (c) and (e), we observe that changes in ΔP_{tot} consistently correlates with the changes (or lack thereof) in E_{seg}. Indeed, when the local pressure changes from compressive to tensile or vice versa from one terrace to the other, the segregation pattern does change accordingly. Additionally, we observe that the magnitude of the change directly correlates with the magnitude in segregation energy. Indeed, in accordance with thermodynamics and the pressure-dependent Langmuir–McLean segregation isotherm [5, 42, 64] which considers the effects of pressure on segregation by estimating the change in segregation enthalpy as $\Delta H_{seg} = (P - P_o) \times \Delta V$, where P is the local pressure, P_o is the background pressure, and ΔV is the change of segregation volume. This isotherm helps us explain that a decrease in the local pressure $\Delta P_{\text{tot}} = P - P_o$ can lower E_{seg} ($\Delta H_{seg} \equiv \Delta E_{seg}$ at zero K) and therefore can induce a change in the segregation behavior as observed for the disconnections studied here. In other words, ΔP_{tot} can be treated as a reliable descriptor for the segregation behavior at disconnections. Similarly, ΔV_{seg} is another important descriptor to determine segregation structures (see Suppl. Fig. S16 in the Supplementary Material), where the antisegregation-to-segregation (same if segregation-to-antisegregation) behavior from the lower to the upper terraces of the disconnection always corresponds to an increase (decrease) of ΔV_{seg}.

By extracting E_{seg}, ΔP_{tot}, and ΔV_{seg} values for each atomic site near the disconnection region within a certain cutoff radius ($R = 1.5$ nm, see insert in Fig. 7 (a)), we can further generalize this relation across all alloy systems. Figure 7 (a) shows the scatter plot of E_{seg} *v.s.* ΔP_{tot} for the faulted disconnections (FD1 and FD2) in the twelve binary alloys. We observe a positive linear correlation between E_{seg} and ΔP_{tot} (Fig. 7 (a)). Owing to the strong linear correlation, we fitted a linear regression model for each E_{seg} *v.s.* ΔP_{tot} per alloy system and then calculated the linear correlation coefficient (denoted as $\tilde{\beta}_{\text{P}}^{\text{A-B}}$, where A is solvent and B is solute). We find that the binary alloys with trilayer-like segregation patterns always have larger $\tilde{\beta}_{\text{P}}^{\text{A-B}}$

values than the binary systems with a single-layer or bilayer-like segregation patterns (Fig. 7 (a)). For instance, $\tilde{\beta}_{\mathrm{P}}^{\mathrm{Cu-Ta}}$ for Cu–Ta is larger than $\tilde{\beta}_{\mathrm{P}}^{\mathrm{Cu-Ni}}$ for Cu–Ni, see Fig. 7 (a). In contrast to its dependence on ΔP_{tot}, the scatter plot in Fig. 7 (b) suggests that E_{seg} is inversely correlated with ΔV_{seg}. It is worthy to note that all above-mentioned behaviors can be found in faulted disconnections for all twelve binary systems (see Suppl. Fig. S17 in the Supplementary Material for more details).

Next, we performed a cluster analysis to further explore the relation between segregation structure and these two descriptors ($\tilde{\beta}_{\mathrm{P}}^{\mathrm{A-B}}$ and $\tilde{\beta}_{\mathrm{V}}^{\mathrm{A-B}}$). Figure 7 (c) shows the scatter plot of $\tilde{\beta}_{\mathrm{P}}^{\mathrm{A-B}}$ *v.s.* $\tilde{\beta}_{\mathrm{V}}^{\mathrm{A-B}}$ for both unfaulted and faulted disconnection configurations for all twelve binary alloys. Interestingly, we can see that when $\tilde{\beta}_{\mathrm{P}}^{\mathrm{A-B}}$ is large and $\tilde{\beta}_{\mathrm{V}}^{\mathrm{A-B}}$ is small, the binary alloys are more likely to have a trilayer-like segregation structure, as it is the case for Cu–Ta and Al–Pb (Fig. 7 (c)). However, when $\tilde{\beta}_{\mathrm{P}}^{\mathrm{A-B}}$ is small and $\tilde{\beta}_{\mathrm{V}}^{A-B}$ is large, the corresponding binary alloys always have less favorable segregation layers, such as single-layer or bilayer-like segregation patterns (Fig. 7 (c)). These observations show that $\tilde{\beta}_{\mathrm{P}}^{\mathrm{A-B}}$ and $\tilde{\beta}_{\mathrm{V}}^{\mathrm{A-B}}$ can be considered as two boundary parameters, inspired from Langmuir–McLean segregation isotherm, that can partition binary alloys into different segregation patterns.

3.5. Relating dislocation character and step height to segregation pattern discontinuity across disconnections

Our analysis thus far showed that the discontinuous segregation patterning across the disconnection is closely related to dislocation character and change in local pressure and that changes in the local stresses are good descriptors for possible changes in the segregation structure. As such, we used our Burgers circuit analysis presented earlier in Fig. 3 to calculate the elastic field corresponding to these disconnection configurations using a continuum line-defect simulation technique. This approach enabled us to connect the dislocation character at the disconnected boundary with the local stress field. Figure 8 (a) shows an illustration of the Volterra construct of a boundary with a disconnection using dislocations and disclination dipoles (see Methods for details). Figures 8 (b-d) show the computed, normalized hydrostatic pressure (σ_{kk}/E) for three representative configuration in Pt, with $\sigma_{kk} = \sigma_{xx}+\sigma_{yy}+\sigma_{zz}$ (σ_{xx}, σ_{yy}, and σ_{zz} are normal stress components in the x, y, and z directions, respectively) alongside with the atomistic segregation maps for Pt–Au.

In the case of the unfaulted configuration UFD1 (Fig. 8 (b)), since there is no Burgers vector component normal to the interface, our FFT-based sim-

ulations described UFD1 as a pure disclination dipole. The calculations confirmed that the hydrostatic pressure is effectively symmetric with respect to the terrace planes. In other words, the upper crystal is mostly in a tensile state (positive pressure), while the lower crystal experiences a compressive state (negative pressure). We note in this case that the simulated stress field closely follows the atomistic segregation energy map, E_{seg},with regions with the highest segregation energies corresponding to the location of the single disclination poles, where the highest stresses are felt. In contrast, looking at the 'interior' and 'exterior' configurations UFD3 (Fig 8 (c)) and FD1 (Fig 8 (d)) respectively, we note that, as a result of the mismatched step heights and non-zero Burgers vectors with respect to the boundary plane direction, the hydrostatic pressure is asymmetric across the terraces. Because these two disconnection configurations have Burgers vector of opposite signs (before dissociation), disclination dipoles and dislocations have also opposite signs. Therefore, we observe that the distribution of negative and positive hydrostatic stresses is opposite between the two configurations confirming our observations in terms of the change in segregating patterns across the disconnection. Here again, the regions with the highest segregation energies corresponds to the regions with the highest stresses.

More interestingly, differences in the dislocation character and step height at these two configurations shed more light on the origin of the discontinuity in segregation patterning. Indeed, for the alloys studied, we can clearly see that the clockwise dislocation rotation in UFD3 corresponds to a segregation-to-antisegregation patterning. The normalized σ_{kk}/E profile of UFD3 configuration shows a large discontinuity at the boundary of positive and negative σ_{kk}/E fields, suggesting the breaking of symmetric hydrostatic pressure (Fig. 8 (c)). Similarly, in the faulted disconnection (FD1), the symmetry of the σ_{kk}/E field can be more easily broken due to the dissociated configuration of the disconnection (see schematic in Fig. 3 (g)), which consists of an inclined stair-rod dislocation ($\boldsymbol{\alpha\delta}$) at the interface, and a stacking fault terminated by a Shockley partial dislocation ($\boldsymbol{\delta}\mathbf{A}$) extending into the upper crystal. This configuration accentuates the segregating pattern, because both disclination dipole and dislocation elastic fields are superimposed with the same signs in the same regions. The various angles associated with the dislocations composing the disconnection map directly to the segregation maps shown in Fig. 5. By comparing the σ_{kk}/E fields between the two distinct 'interior' and 'exterior' $1/3\langle 111\rangle$ disconnections, UFD3 and FD1, we note that the sign of the hydrostatic pressure is directly linked to the orientation

of the dislocation sitting at the step region, as a primary parameter, and to the Frank vector sign as a secondary parameter. In fact our defect-based continuum micromechanics simulations also highlight the role of the size of the dislocation core at the step region. A rapid parametric study showed that the magnitude of the hydrostatic stress field can be changed by varying the area A spread by the defect core (*i.e.* varying the defect density involved in the numerical simulations (See Methods for description of model).

Clearly, the distribution of local stresses near the disconnection is controlled by its character in terms of step height (embodied by the disclination dipole length in our FFT-based continuum mechanics calculations), the orientation of the dislocation sitting at that step region of the disconnection, the magnitude of the Burgers vector, and in some cases, the presence of a stacking fault (for the faulted configurations). While these effects cannot be separated in our atomistic models, our FFT-based dislocation-disclination simulations enable us to test various hypothetical disconnection configurations as combinations of dislocation and disclination type defects from the Volterra construct. These hypothetical constructs isolate the respective roles of the dislocation character and step height on the stress field, *de facto* explaining changes in the segregation pattern via the ΔP_{tot} atomistic descriptor (see Fig. 6 and Section 3.4).

We show in Fig. 9 the effect of step height by comparing the stress fields of two representative unfaulted disconnections, UFD1 and UFD3, with their hypothetical counterparts in the absence of a step ($h_{\text{step}} = 0$ nm) or for a larger step ($h_{\text{step}} = 1.0$ nm). In these simulations, the character of the dislocation sitting at the step region of the disconnection was kept identical to the actual configuration from our atomistic results. In the case of UFD1 (see Fig. 9 (a)), this comparison illustrates the fact that the local stress field near the step region remains similar, but a large positive and negative stress fields appeared near the disclination single poles (black and white triangles) for the disconnection with a larger h_{step}. A similar observation can be also found with the UFD3 configuration (Fig. 9 (b)) for which the dislocation is rotated by 90° as compared to the UFD1 configuration. These results show that a larger disconnection step increases the magnitude and the extent of the stress field. In fact, these results illustrate the role of the disconnection step acting as an internal (elastic) length scale dictating the extend of the stress field near the disconnection.

Figure 10 further completes the above conclusion by illustrating the effect of the orientation of the dislocation at the step region and the possible syn-

ergistic or antagonistic effects with step height. In this figure, we considered three representative disconnections, *i.e.* UFD1, UFD3, and FD1, with hypothetical configurations with or without the dislocation being rotated with respect to the terraces' planes. Several observations can be drawn. Clearly, regardless of the configuration considered, when no rotation of the dislocation sitting is considered (see panel (a)), we observe that the hydrostatic stress fields near the step region are negative in the upper crystal C_λ and positive in the lower crystal C_μ, preserving the symmetrical distribution of stresses across the disconnection (*i.e.* $\Delta P_{\text{tot}} = 0$). However, once the dislocation undergoes a rotation in UFD1 and FD1 (see panel (b)), the local hydrostatic stress fields become positive near one terrace for both the upper and lower crystals but is negative near the other terrace, therefore forming an asymmetrical field across the disconnection. The presence of the stacking fault does not change these observations. An interesting additional observation here can be noted for the faulted FD1 configurations (original and hypothetical), for which we note that in the hypothetical 'no rotation' case (which would correspond to another disconnection Burgers vector), while the stress is symmetrical across the disconnection, the dislocation sitting at the step tends to counteract and suppress the stress field from the step coming from the disclination dipole.

This synergistic/antagonistic effect is further exemplified in Fig. 11. In this figure, we show the combined effects of the step and the stacking fault for the hypothetical faulted FD1 configurations. Panel (a) illustrates the fact that the presence of a step has little effect as compared to the presence of the stacking fault and associated trailing partial. Indeed, we observed that the distribution of local stresses is relatively similar and dominated by the Shockley partial that was emitted from the step region. In this case, one would expect that, in addition to the break of symmetry in the local stress field induced by the presence of the dislocation at the step, the stacking fault would accentuate the segregation effect near the upper terrace. However in panel (b) illustrates the effect of the separation between the Shockley partial and the step and the aforementioned internal (elastic) length scale associated with the step and the synergistic effect of the dislocation and step height. As expected, stress concentration effects are more prominent and amplified when the partial sits closer to the step region. In this case, one would expect that the separation distance between the partial and the step region, reinforced by the stress field from the dislocation at the step, would dictate the intensity of pressure-induced segregation effects near the upper terrace.

4. Conclusion

In conclusion, this work reveals the possibility of discontinuous solute segregation patterns across different $\Sigma3(111)$ twin-based disconnections for a broad range of binary alloys. This phenomenon appears to be ubiquitous across the various boundary configurations and alloy systems investigated, and is observed regardless of the initial segregating pattern (single-layer occupation; bi- and trilayer occupation) for the reference, pristine, defect-free twin boundary. Continuum-based theoretical predictions confirmed our atomistic analysis on the origin of the change in the segregation patterns which is rooted in the orientation and character of the dislocation sitting at the step region and how it interacts with the intrinsic stress field of the step itself. Although, prior studies usually used descriptors such as atomic size mismatch or ratio of electronegativity to capture the solute segregation at boundaries [26], our analysis shows that, in the case of disconnected boundaries, the disconnection characteristics dominates the segregation strength. In this case, the relevant descriptors describing the local segregation behavior are the local pressure drop and segregation volume ($\tilde{\beta}_{\mathrm{P}}^{\mathrm{A-B}}$ and $\tilde{\beta}_{\mathrm{V}}^{\mathrm{A-B}}$) along with the normalized hydrostatic stress σ_{kk}/E. These descriptors are consistent with the pressure-dependent Langmuir–McLean segregation isotherm used to describe the thermodynamics of interfacial segregation[5]. In addition, we show that the actual break of symmetry across the boundary terraces should be sufficient to trigger a change from one segregation pattern to another. Since dissociated boundary structures[35, 65, 66] and various spatial arrangements of dislocation structures at boundaries[67–69] have been widely observed for many grain boundaries, we anticipate that the discontinuous segregation patterning reported in this work should exist for many different types of grain boundaries. Although the focus of this study was on FCC metallic alloys, we also expect that similar principles would apply to other metallic alloys, ceramics, and semiconductors.

These findings enrich our current understanding of the stability of nanocrystalline systems[70–72]. For instance, it has been recently reported that grain boundaries can actually have their own miscibility gaps, altering the segregation behavior in nanocrystalline alloys [73], especially in the presence of grain-boundary defects such as disconnections, and therefore affecting their thermal stability. The present results enrich such descriptions by showing that, in addition to a boundary-specific miscibility gap, specific disconnection configurations can further create a structurally inhomogeneous land-

scape influencing the segregating behavior along generic boundary segments. Additionally, our observations on synergistic/antagonistic effects between the dislocation and step at the disconnection offer a connection (in the present case a disconnection!) with the Cottrell atmosphere theory [17, 25] if one were to consider the near- and far-field elastic effects (disconnection *vs.* dislocation *vs.* step) within this theoretical framework to elastically deformed lattice regions around the disconnection and form a non-trivial Cottrell atmosphere. The spatial confinement and manipulation of segregation states via disconnections offer new research directions to explore the design of alloys with improved strength, ductility, damage tolerance, and other functional properties. In this context, selective and graded solute patterning [74] married with disconnection-like attributes could open up new perspectives for the development of functionally graded microstructures.

Data availability

The database for segregation of all binary alloys, in the form of LAMMPS text dump files is available from the authors upon request.

Code availability

An example of LAMMPS input file with all parameters to run the segregation simulations is available from the authors upon request.

References

[1] J. W. Christian, S. Mahajan, Deformation twinning, Prog. Mater. Sci. 39 (1) (1995) 1–157. doi:10.1016/0079-6425(94)00007-7.

[2] Y. T. Zhu, X. Z. Liao, X. L. Wu, Deformation twinning in nanocrystalline materials, Prog. Mater. Sci. 57 (1) (2012) 1–62. doi:10.1016/j.pmatsci.2011.05.001.

[3] J. P. Hirth, J. Wang, C. N. Tomé, Disconnections and other defects associated with twin interfaces, Prog. Mater. Sci. 83 (2016) 417–471. doi:10.1016/j.pmatsci.2016.07.003.

[4] P. R. Cantwell, M. Tang, S. J. Dillon, J. Luo, G. S. Rohrer, M. P. Harmer, Grain boundary complexions, Acta Mater. 62 (2014) 1–48. doi:10.1016/j.actamat.2013.07.037.

[5] P. Lejček, L. Zheng, S. Hofmann, M. Šob, Applied thermodynamics: Grain boundary segregation, Entropy 16 (3) (2014) 1462–1483. doi:h10.3390/e16031462.

[6] C. Hu, Y. Zuo, C. Chen, S. Ong, J. Luo, Genetic algorithm-guided deep learning of grain boundary diagrams: Addressing the challenge of five degrees of freedom, Mater. Today 38 (2020) 49–57. doi:10.1016/j.mattod.2020.03.004.

[7] D. Aksoy, R. Dingreville, D. Spearot, Spectrum of embrittling potencies and relation to properties of symmetric-tilt grain boundaries, Acta Mater. 205 (2021) 116527. doi:10.1016/j.actamat.2020.116527.

[8] M. E. Fernandez, R. Dingreville, D. E. Spearot, Statistical perspective on embrittling potency for intergranular fracture, Phys. Rev. Mater. 6 (8) (2022) 083602. doi:10.1103/PhysRevMaterials.6.083602.

[9] E. A. Jägle, E. J. Mittemeijer, The kinetics of grain-boundary nucleated phase transformations: Simulations and modelling, Acta Mater. 59 (14) (2011) 5775–5786. doi:10.1016/j.actamat.2011.05.054.

[10] J. Han, S. L. Thomas, D. J. Srolovitz, Grain-boundary kinetics: A unified approach, Prog. Mater. Sci. 98 (2018) 386–476. doi:10.1016/j.pmatsci.2018.05.004.

[11] W. Barrows, R. Dingreville, D. Spearot, Traction–separation relationships for hydrogen induced grain boundary embrittlement in nickel via molecular dynamics simulations, Mater. Sci. Eng. A 650 (2016) 354–364. doi:10.1016/j.msea.2015.10.042.

[12] C. Hu, Y. Li, Z. Yu, J. Luo, Computing grain boundary diagrams of thermodynamic and mechanical properties, npj Comput. Mater. 7 (1) (2021) 1–12. doi:10.1038/s41524-021-00625-2.

[13] C. Xiang, M. Shen, C. Hu, L. W. Wong, H. Nie, H. Lei, J. Luo, J. Zhao, Z. Yu, Atomistic observation of in situ fractured surfaces at a V-doped WC–Co interface, J. Mater. Sci. Technol. 110 (2022) 103–108. doi:10.1016/j.jmst.2021.09.021.

[14] H. Bishara, S. Lee, T. Brink, M. Ghidelli, G. Dehm, Understanding grain boundary electrical resistivity in Cu: the effect of boundary structure, ACS Nano 15 (10) (2021) 16607–16615. doi:10.1021/acsnano.1c06367.

[15] J. Brown, Y. Mishin, Segregation and structural transformations at $\Sigma = 3$ grain boundaries in NiAl: A Monte-Carlo study, Acta Mater. 53 (7) (2005) 2149–2156. doi:10.1016/j.actamat.2005.01.027.

[16] R. Sun, Z. Wang, M. Saito, N. Shibata, Y. Ikuhara, Atomistic mechanisms of nonstoichiometry-induced twin boundary structural transformation in titanium dioxide, Nat. Commun. 6 (1) (2015) 1–7. doi:10.1038/ncomms8120.

[17] R. Dingreville, S. Berbenni, On the interaction of solutes with grain boundaries, Acta Mater. 104 (2016) 237–249. doi:10.1016/j.actamat.2015.11.017.

[18] Z. Pan, T. Rupert, Effect of grain boundary character on segregation-induced structural transitions, Phys. Rev. B 93 (13) (2016) 134113. doi:10.1103/PhysRevB.93.134113.

[19] P. R. Cantwell, T. Frolov, T. J. Rupert, A. R. Krause, C. J. Marvel, G. S. Rohrer, J. M. Rickman, M. P. Harmer, Grain boundary complexion transitions, Annu. Rev. Mater. Res. 50 (2020) 465–492. doi:10.1146/annurev-matsci-081619-114055.

[20] T. Meiners, T. Frolov, R. E. Rudd, G. Dehm, C. H. Liebscher, Observations of grain-boundary phase transformations in an elemental metal, Nature 579 (7799) (2020) 375–378. doi:10.1038/s41586-020-2082-6.

[21] N. Zhou, C. Hu, J. Luo, Grain boundary segregation transitions and critical phenomena in binary regular solutions: A systematics of complexion diagrams with universal characters, Acta Mater. 221 (2021) 117375. doi:10.1016/j.actamat.2021.117375.

[22] S.-M. Kuo, A. Seki, Y. Oh, D. N. Seidman, Solute-atom segregation: An oscillatory Ni profile at an internal interface in Pt (Ni), Phys. Rev. Lett. 65 (2) (1990) 199. doi:10.1103/PhysRevLett.65.199.

[23] J. F. Nie, Y. M. Zhu, J. Z. Liu, X.-Y. Fang, Periodic segregation of solute atoms in fully coherent twin boundaries, Science 340 (6135) (2013) 957–960. doi:10.1126/science.122936.

[24] W. Cai, R. B. Sills, D. M. Barnett, W. D. Nix, Modeling a distribution of point defects as misfitting inclusions in stressed solids, J. Mech. Phys. Solids 66 (2014) 154–171. doi:10.1016/j.jmps.2014.01.015.

[25] Y. Mishin, J. W. Cahn, Thermodynamics of Cottrell atmospheres tested by atomistic simulations, Acta Mater. 117 (2016) 197–206. doi:10.1016/j.actamat.2016.07.013.

[26] J. Startt, R. Dingreville, S. Raiman, C. Deo, An electronic origin to the oscillatory segregation behavior in Ni-Cr and other BCC defects in FCC metals, Acta Mater. 218 (2021) 117215. doi:10.1016/j.actamat.2021.117215.

[27] Z. Luo, C. Hu, L. Xie, H. Nie, C. Xiang, X. Gu, J. He, W. Zhang, Z. Yu, J. Luo, A highly asymmetric interfacial superstructure in WC: Expanding the classic grain boundary segregation and new complexion theories, Mater. Horiz. 7 (1) (2020) 173–180. doi:10.1039/C9MH00969H.

[28] C. Yang, C. Hu, C. Xiang, H. Nie, X. Gu, L. Xie, J. He, W. Zhang, Z. Yu, J. Luo, Interfacial superstructures and chemical bonding transitions at metal-ceramic interfaces, Sci. Adv. 7 (11) (2021) eabf6667. doi:10.1126/sciadv.abf6667.

[29] Y. Jiang, H. Li, T. Yao, Y. Wang, D. Yin, C. Chen, X. Ma, H. Ye, Y. Ikuhara, Spin polarization-assisted dopant segregation at a coherent phase boundary, ACS Nano 15 (12) (2021) 19938–19944. doi:10.1021/acsnano.1c07449.

[30] J. P. Hirth, R. C. Pond, Steps, dislocations and disconnections as interface defects relating to structure and phase transformations, Acta Mater. 44 (12) (1996) 4749–4763. doi:10.1016/S1359-6454(96)00132-2.

[31] X.-Y. Sun, C. Fressengeas, V. Taupin, P. Cordier, N. Combe, Disconnections, dislocations and generalized disclinations in grain boundary ledges, Int. J. Plast. 104 (2018) 134–146. doi:10.1016/j.ijplas.2018.02.003.

[32] C. M. Barr, E. Y. Chen, J. E. Nathaniel II, P. Lu, D. P. Adams, R. Dingreville, B. L. Boyce, K. Hattar, D. L. Medlin, Irradiation-induced grain boundary facet motion: In situ observations and atomic-scale mechanisms, Sci. Adv. 8 (23) (2022) abn0900. doi:10.1126/sciadv.abn0900.

[33] J. P. Hirth, Dislocations, steps and disconnections at interfaces, J. Phys. Chem. Solids 55 (10) (1994) 985–989. doi:10.1016/0022-3697(94)90118-X.

[34] M. Shamzuzzoha, P. A. Deymier, D. J. Smith, A high-resolution electron microscopy study of secondary dislocations in Σ= 3, $[\bar{1}10]$–$(\bar{1}\bar{1}1)$ grain boundaries of aluminium, Philos. Mag. A 64 (1) (1991) 245–253. doi:10.1080/01418619108206138.

[35] K. L. Merkle, Atomic structure of grain boundaries, J. Phys. Chem. Solids 55 (10) (1994) 991–1005. doi:10.1016/0022-3697(94)90119-8.

[36] D. L. Medlin, C. B. Carter, J. E. Angelo, M. J. Mills, Climb and glide of a/3$\langle 111\rangle$ dislocations in an aluminium Σ= 3 boundary, Philos. Mag. A 75 (3) (1997) 733–747. doi:10.1080/01418619708207199.

[37] E. A. Marquis, D. L. Medlin, Structural duality of 1/3 $\langle 111\rangle$ twin-boundary disconnections, Philos. Mag. Lett. 85 (8) (2005) 387–394. doi:10.1080/09500830500311697.

[38] S. Akarapu, H. Zbib, J. P. Hirth, Modeling and analysis of disconnections in tilt walls, Scripta Mater. 59 (3) (2008) 265–267. doi:10.1016/j.scriptamat.2008.02.049.

[39] J. Wang, I. J. Beyerlein, C. N. Tomé, An atomic and probabilistic perspective on twin nucleation in Mg, Scripta Mater. 63 (7) (2010) 741–746. doi:10.1016/j.scriptamat.2010.01.047.

[40] S. Dai, Y. Xiang, T.-Y. Zhang, A continuum model for core relaxation of incoherent twin boundaries based on the Peierls–Nabarro framework, Scripta Mater. 64 (5) (2011) 438–441. doi:10.1016/j.scriptamat.2010.11.008.

[41] C. J. O'Brien, D. L. Medlin, S. M. Foiles, Misoriented grain boundaries vicinal to the twin in nickel Part I: Thermodynamics & temperature-dependent structure, Philos. Mag. 96 (13) (2016) 1285–1304. doi:10.1080/14786435.2016.1161862.

[42] C. Hu, D. L. Medlin, R. Dingreville, Disconnection-mediated transition in segregation structures at twin boundaries, J. Phys. Chem. Lett. 12 (29) (2021) 6875–6882. doi:10.1021/acs.jpclett.1c02189.

[43] S. Plimpton, Fast parallel algorithms for short-range molecular dynamics, J. Comp. Phys. 117 (1) (1995) 1–19. doi:10.1006/jcph.1995.1039.

[44] A. Landa, P. Wynblatt, D. J. Siegel, J. B. Adams, O. N. Mryasov, X.-Y. Liu, Development of glue-type potentials for the Al–Pb system: Phase diagram calculation, Acta Mater. 48 (8) (2000) 1753–1761. doi:10.1016/S1359-6454(00)00002-1.

[45] M. I. Mendelev, M. Asta, M. J. Rahman, J. J. Hoyt, Development of interatomic potentials appropriate for simulation of solid–liquid interface properties in Al–Mg alloys, Philos. Mag. 89 (34-36) (2009) 3269–3285. doi:10.1080/14786430903260727.

[46] H.-S. Nam, D. J. Srolovitz, Molecular dynamics simulation of Ga penetration along Σ5 symmetric tilt grain boundaries in an Al bicrystal, Phys. Rev. B 76 (18) (2007) 184114. doi:10.1103/PhysRevB.76.184114.

[47] F. Fischer, G. Schmitz, S. M. Eich, A systematic study of grain boundary segregation and grain boundary formation energy using a new copper–nickel embedded-atom potential, Acta Mater. 176 (2019) 220–231. doi:10.1016/j.actamat.2019.06.027.

[48] M. I. Mendelev, Y. Sun, F. Zhang, C.-Z. Wang, K.-M. Ho, Development of a semi-empirical potential suitable for molecular dynamics simulation of vitrification in Cu–Zr alloys, J. Chem. Phys. 151 (21) (2019) 214502. doi:10.1063/1.5131500.

[49] P. L. Williams, Y. Mishin, J. C. Hamilton, An embedded-atom potential for the Cu–Ag system, Model. Simul. Mat. Sci. Eng. 14 (5) (2006) 817–833. doi:10.1088/0965-0393/14/5/002.

[50] G. D. Samolyuk, L. K. Béland, G. M. Stocks, R. E. Stoller, Electron–phonon coupling in Ni-based binary alloys with application to displacement cascade modeling, J. Phys.: Condens. Matt. 28 (17) (2016) 175501. doi:10.1088/0953-8984/28/17/175501.

[51] W. S. R., M. I. Mendelev, Anisotropy of the solid–liquid interface properties of the Ni–Zr B33 phase from molecular dynamics simulation, Philos. Mag. 95 (2) (2015) 224–241. doi:10.1080/14786435.2014.995742.

[52] C. J. O'Brien, C. M. Barr, P. M. Price, K. Hattar, S. M. Foiles, Grain boundary phase transformations in PtAu and relevance to thermal stabilization of bulk nanocrystalline metals, J. Mater. Sci. 53 (4) (2018) 2911–2927. doi:10.1007/s10853-017-1706-1.

[53] J.-S. Kim, D. Seol, J. Ji, H.-O. Jang, Y. Kim, B.-J. Lee, Second nearest-neighbor modified embedded-atom method interatomic potentials for the Pt-M (M = Al, Co, Cu, Mo, Ni, Ti, V) binary systems, Calphad 59 (2017) 131–141. doi:10.1016/j.calphad.2017.09.005.

[54] J.-H. Shim, K.-H. Ko, W.-S.and Kim, H.-S. Lee, Y.-S. Lee, J.-Y. Suh, Y. W. Cho, B.-J. Lee, Prediction of hydrogen permeability in V–Al and V–Ni alloys, J. Membr. Sci. 430 (2013) 234–241. doi:10.1016/j.memsci.2012.12.019.

[55] G. P. P. Pun, K. A. Darling, L. J. Kecskes, Y. Mishin, Angular-dependent interatomic potential for the Cu-Ta system and its application to structural stability of nano-crystalline alloys, Acta Mater. 100 (2015) 377–391. doi:10.1016/j.actamat.2015.08.052.

[56] C. A. Becker, F. Tavazza, Z. T. Trautt, R. A. Buarque de Macedo, Considerations for choosing and using force fields and interatomic potentials in materials science and engineering, Curr. Opin. Solid State Mater. Sci. 17 (6) (2013) 277–283. doi:10.1016/j.cossms.2013.10.001.

[57] C. L. Kelchner, S. J. Plimpton, J. C. Hamilton, Dislocation nucleation and defect structure during surface indentation, Phys. Rev. B 58 (17) (1998) 11085. doi:10.1103/PhysRevB.58.11085.

[58] A. Stukowski, Visualization and analysis of atomistic simulation data with OVITO–the Open Visualization Tool, Model. Simul. Mater. Sci. Eng. 18 (1) (2009) 015012. doi:10.1088/0965-0393/18/1/015012.

[59] S. Berbenni, V. Taupin, K. S. Djaka, C. Fressengeas, A numerical spectral approach for solving elasto-static field dislocation and g-disclination mechanics, Int. J. Solids Struct. 51 (23-24) (2014) 4157–4175. doi:10.1016/j.ijsolstr.2014.08.009.

[60] S. Berbenni, V. Taupin, Fast Fourier transform-based micromechanics of interfacial line defects in crystalline materials, J Micromech. Mol. Phys. 3 (03n04) (2018) 1840007. doi:10.1142/S2424913018400076.

[61] J. P. Hirth, R. C. Pond, J. Lothe, Disconnections in tilt walls, Acta Mater. 54 (16) (2006) 4237–4245. doi:10.1016/j.actamat.2006.05.017.

[62] J. Ahrens, B. Geveci, C. Law, Paraview: An end-user tool for large data visualization, The Visualization Handbook 717 (8) (2005). doi:10.1016/B978-012387582-2/50038-1.

[63] S. M. Foiles, D. L. Medlin, Structure and climb of 1/3 ⟨111⟩ twin dislocations in aluminum, Mater. Sci. Eng. A 319-321 (2001) 102–106. doi:10.1016/S0921-5093(01)01112-1.

[64] T.-Y. Zhang, H. Ren, Solute concentrations and strains in nanograined materials, Acta Mater. 61 (2) (2013) 477–493. doi:10.1016/j.actamat.2012.09.060.

[65] F. Ernst, M. W. Finnis, D. Hofmann, T. Muschik, U. Schönberger, U. Wolf, M. Methfessel, Theoretical prediction and direct observation of the 9R structure in Ag, Phys. Rev. Lett. 69 (1992) 620–623. doi:10.1103/PhysRevLett.69.620.

[66] J. D. Rittner, D. N. Seidman, K. L. Merkle, Grain-boundary dissociation by the emission of stacking faults, Phys. Rev. B 53 (8) (1996) R4241. doi:10.1103/PhysRevB.53.R4241.

[67] D. A. Hughes, N. Hansen, D. J. Bammann, Geometrically necessary boundaries, incidental dislocation boundaries and geometrically necessary dislocations, Scripta Mater. 48 (2) (2003) 147–153. doi:10.1016/S1359-6462(02)00358-5.

[68] C. Moussa, M. Bernacki, R. Besnard, N. Bozzolo, Statistical analysis of dislocations and dislocation boundaries from EBSD data, Ultramicroscopy 179 (2017) 63–72. doi:10.1016/j.ultramic.2017.04.005.

[69] G. Winther, X. Huang, Dislocation structures. Part II. Slip System Dependence, Philos. Mag. 87 (33) (2007) 5215–5235. doi:10.1080/14786430701591505.

[70] T. Chookajorn, H. A. Murdoch, C. A. Schuh, Design of stable nanocrystalline alloys, Science 337 (6097) (2012) 951–954. doi:10.1126/science.1224737.

[71] D. Raabe, M. Herbig, S. Sandlöbes, Y. Li, D. Tytko, M. Kuzmina, D. Ponge, P.-P. Choi, Grain boundary segregation engineering in metallic alloys: A pathway to the design of interfaces, Curr. Opin. Solid State Mater. Sci. 18 (4) (2014) 253–261. doi:10.1016/j.cossms.2014.06.002.

[72] A. R. Kalidindi, C. A. Schuh, Stability criteria for nanocrystalline alloys, Acta Mater. 132 (2017) 128–137. doi:10.1016/j.actamat.2017.03.029.

[73] X. Zhou, R. D. Kamachali, B. L. Boyce, B. G. Clark, D. Raabe, G. B. Thompson, Spinodal decomposition in nanocrystalline alloys, Acta Mater. 215 (2021) 117054. doi:10.1016/j.actamat.2021.117054.

[74] J. M. Monti, E. M. Hopkins, K. Hattar, F. Abdeljawad, B. L. Boyce, R. Dingreville, Stability of immiscible nanocrystalline alloys in compositional and thermal fields, Acta Mater. 226 (2022) 117620. doi:10.1016/j.actamat.2022.117620.

Acknowledgements

The authors would like to thanks B.L. Boyce from Sandia National Laboratories for suggestions and comments on the manuscript. C.H., D.M., and R.D. are supported by the United States (U.S.) Department of Energy (DOE) Office of Basic Energy Sciences (BES), Department of Materials Science and Engineering. S.B. is supported by the French State through the program "Investment in the future" operated by the National Research Agency (ANR) and referenced by ANR-11-LABX-0008-01 (Laboratory of Excellence 'DAMAS': Design of Alloy Metals for low-mAss Structures). Computational resources are supported by the Center for Integrated Nanotechnologies, an Office of Science User Facility operated for the U.S. Department of Energy. Sandia National Laboratories is a multi-mission laboratory managed and operated by National Technology and Engineering Solutions of Sandia, LLC, a

wholly owned subsidiary of Honeywell International, Inc., for the U.S. Department of Energy's National Nuclear Security Administration under contract DE-NA0003525. The views expressed in this article do not necessarily represent the views of the U.S. Department of Energy or the United States Government. This article has been authored by an employee of National Technology & Engineering Solutions of Sandia, LLC under Contract No. DE-NA0003525 with the U.S. Department of Energy (DOE). The employee owns all right,title and interest in and to the article and is solely responsible for its contents. The United States Government retains and the publisher, by accepting the article for publication, acknowledges that the United States Government retains a non-exclusive, paid-up, irrevocable, world-wide license to publish or reproduce the published form of this article or allow others to do so, for United States Government purposes. The DOE will provide public access to these results of federally sponsored research in accordance with the DOE Public Access Plan https://www.energy.gov/downloads/doe-public-access-plan.

Author contributions

C.H. and R.D. proposed the research idea and designed the overall study. C.H. performed the atomistic simulations. D.M. advised on the dislocation analysis. S.B. performed the continuum-based field dislocation and disclination mechanics simulations. R.D. provided overall guidance. All the authors analyzed the data, discussed the results, and contributed to writing and reviewing the manuscript.

Competing interests

The authors declare no competing interests.

Materials & Correspondence

Requests and correspondence should be addressed to R. Dingreville.

Additional information

Additional information are available in the **Supplementary Material** regarding (i) the disconnection atomic structures (Note 1) for pristine Cu,

Al, and Ni (*i.e.* no solute), (iv) the Burgers circuit analysis for all disconnection configurations (Note 2), (iii) profiles of the segregation energy for all twelve binary alloys simulated (Note 3), and (iv) calculation of the segregation volumes and correlations for all twelve binary alloys simulated (Note 4).

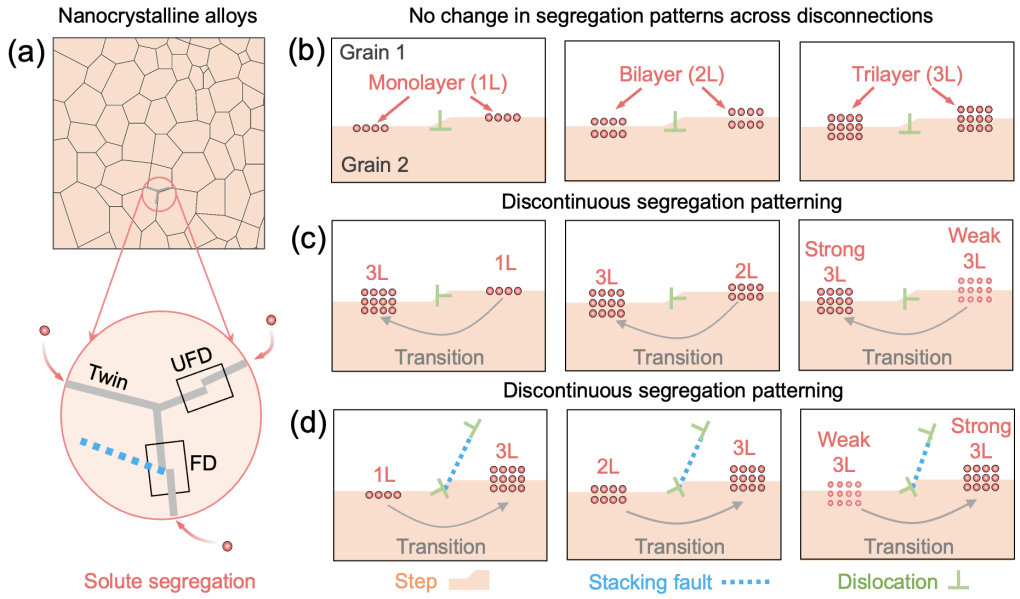

Figure 1: **Discontinuous segregation patterning at grain boundary disconnections.** (a) schematic diagram of nanotwinned grains in nanocrystalline alloys. The insert displays the faulted disconnection (FD) with stacking fault (blue dashed line) and unfaulted disconnection (UFD) without a stacking fault. The red atoms represent solute atoms which generally segregate to the grain-boundary region in binary alloys. (b)–(d) Schematic diagrams for the segregation patterning at a disconnected twin boundary. Segregation patterns can change from single-layer (1L) to bilayer (2L) to tri/multi-layers (3L). In (b), no change in the segregation pattern is expected on either side of the terraces composing the disconnection. The dislocation present at the step region does not break the local symmetry. The lower and upper terraces for the UFD structures have the same segregation pattern as the pristine twin boundary when there is no rotation of the dislocation (green symbol). In (c) and (d), segregation patterns change across the disconnection due to the rotation of the dislocation at the step region (c) and the emission a stacking fault (d) that resulted in a break of the symmetry. When the dislocation rotates in the UFD, the lower and upper terraces of FD structures always have discontinuous segregation patterns.

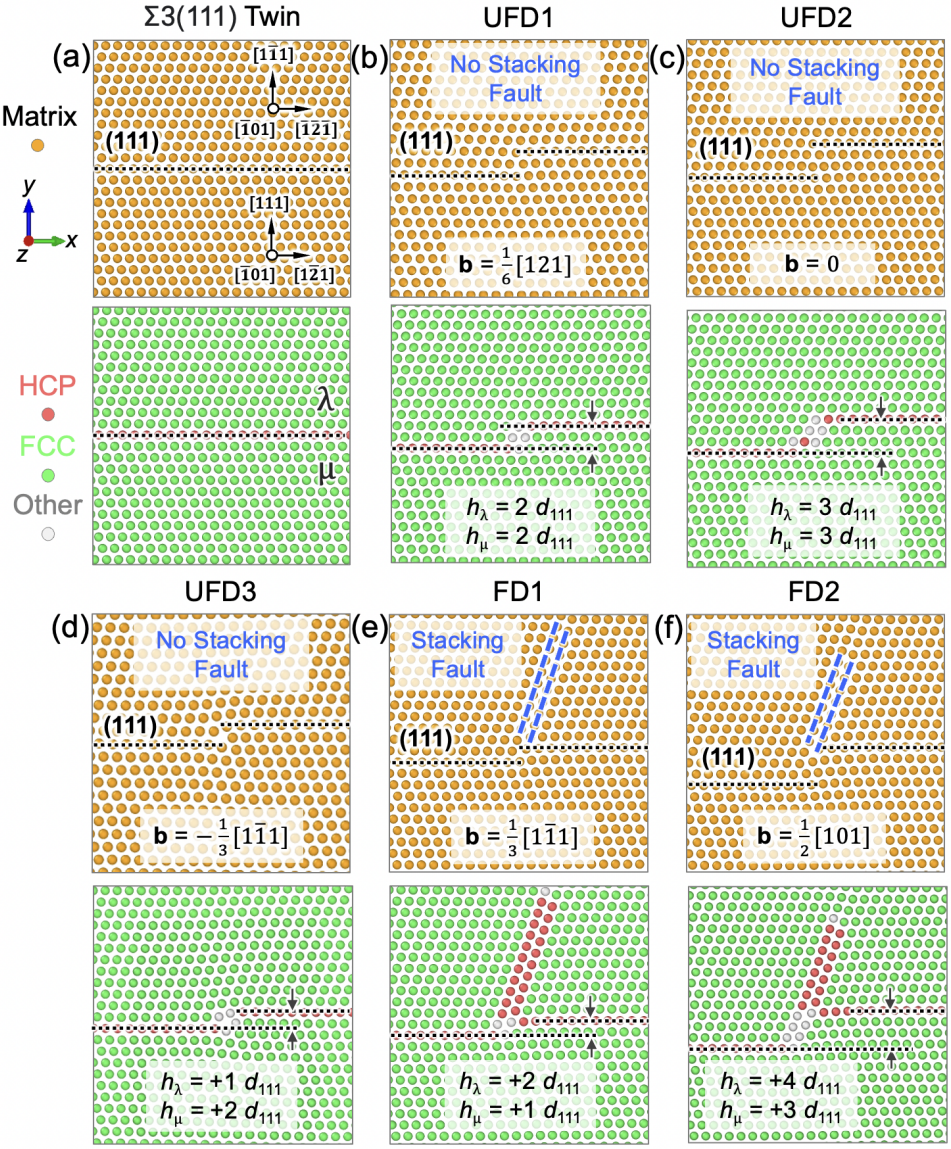

Figure 2: **Atomistic structure of the Σ3(111) twin boundary and corresponding disconnections**. MD-relaxed atomistic structure and common neightbor analysis (CNA) of (a) pristine Σ3(111) twin boundary, (b-d) three types of unfaulted disconnections (UFD) with different step heights, h_{step}, and Burgers vector, **b**, and (e-f) faulted disconnections (FD) with different h and **b** in Pt.

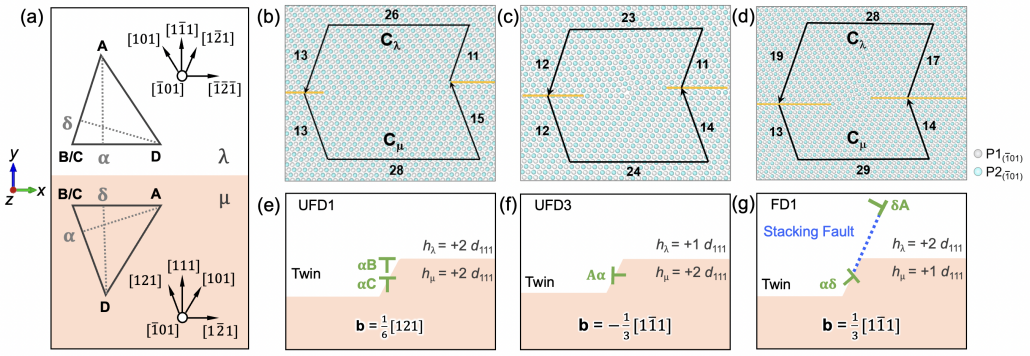

Figure 3: **Dislocation analysis for three representative disconnections**. (a) Schematic illustration of the coordinate frames and projection of the Thompson's tetrahedra for the upper (λ) and lower (μ) crystals. Burgers circuit analysis of dislocations for (b) UFD1, (c) UFD3, and (d) FD1 disconnections. The schematic illustrations of the dislocation configurations are provided for (e) UFD1, (f) UFD3, and (g) FD1 disconnections. Note that for the UFD1 configuration in (e) the two dislocations $\boldsymbol{\alpha}\mathbf{B}$ and $\boldsymbol{\alpha}\mathbf{C}$ can be represented as a single dislocation $\mathbf{D}\boldsymbol{\alpha} = \boldsymbol{\alpha}\mathbf{B} + \boldsymbol{\alpha}\mathbf{C}$.

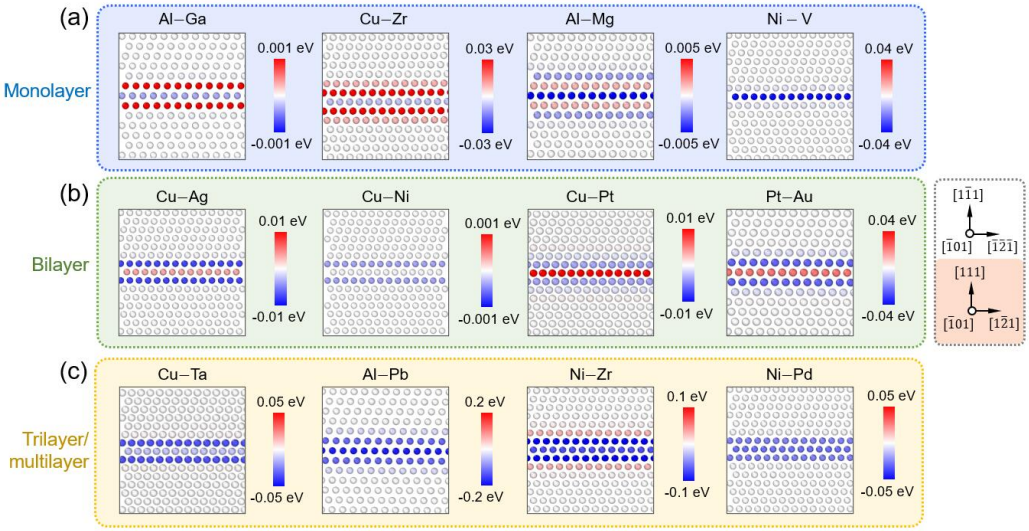

Figure 4: **Segregation energy map, E_{seg}, for the defect-free Σ3(111) twin boundary for twelve A-B alloys**. Three types of segregation patterns can be identified: (a) single-layer (1L)-like segregation pattern, where the boundary layer of Σ3(111) twin has negative E_{seg} (blue color) and adjacent two layers have positive E_{seg} (red color). (b) alternating bilayer (2L)-like segregation pattern, where the boundary layer of Σ3(111) twin has positive E_{seg} and subsequent two layers exhibit negative E_{seg}. (c) trilayer (3L)- or multilayer-like segregation patterns, where all three (or more) layers at the boundary region have negative E_{seg}. Negative E_{seg} (blue color) indicates a segregating site while positive E_{seg} (red color) indicates an anti-segregating site. For each binary system (A–B), the matrix element (A) has a face-centered-cubic (FCC) structure regardless of the solute type. (For interpretation of the colors in the figure(s), the reader is referred to the web version of this article.)

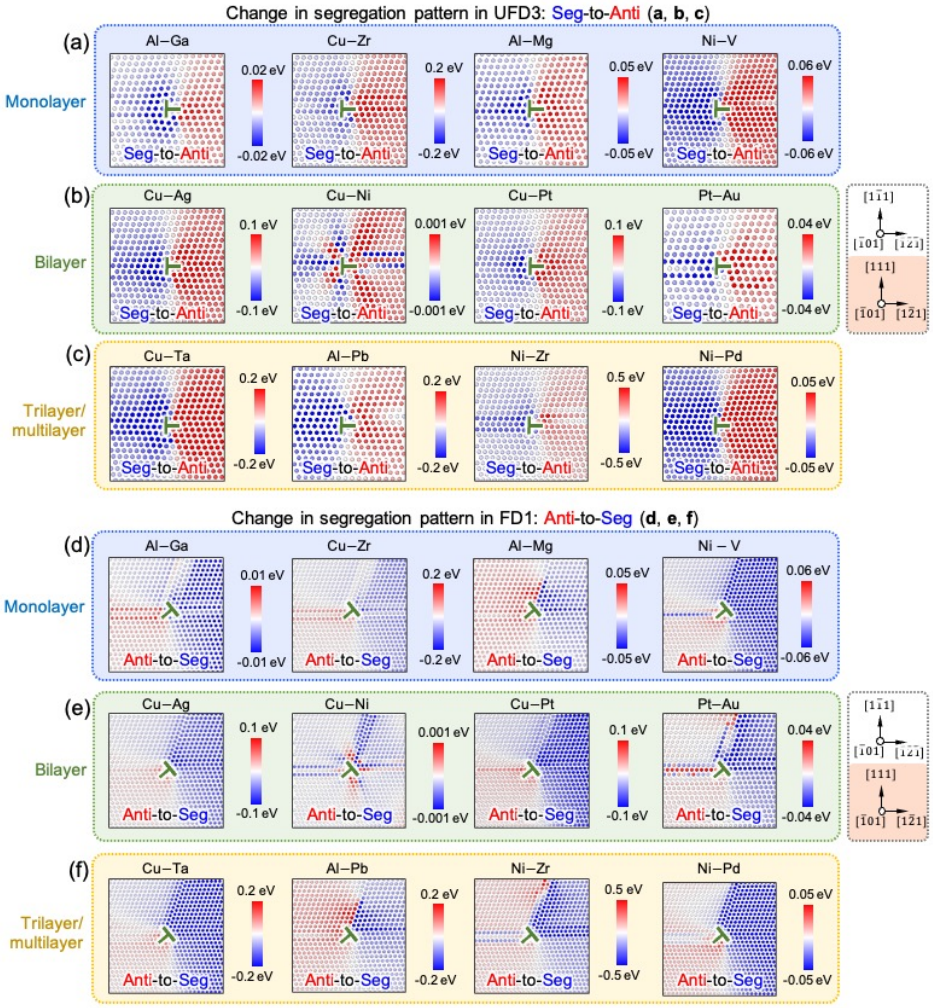

Figure 5: **Discontinuous segregation patterning in unfaulted and faulted disconnections**. Segregation energy maps, E_{seg}, of (a) single-layer (1L)-like, (b) bilayer (2L)-like, and (c) trilayer (3L) or multilayer-like segregation patterns near the unfaulted disconnection, UFD3. The segregation patterns in UFD3 undergo segregation-to-anti-segregation variation from the lower terrace region (blue color) to the upper terrace region (red color). E_{seg} maps of (d) single-layer (1L)-like, (e) bilayer (2L)-like, and (f) trilayer (3L) or multilayer-like segregation patterns for the faulted disconnection, FD1. The segregation patterns in FD1 have an anti-segregation-to-segregation variation from the lower terrace region (red color) to the upper terrace region (blue color). Note that for the FD1 structures, only the stair-rod part of the disconnection ($\boldsymbol{\alpha\delta}$) has been annotated and not the Shockley partial ($\boldsymbol{\delta A}$) in the upper crystal, see schematics in Fig. 4 for full configurations.

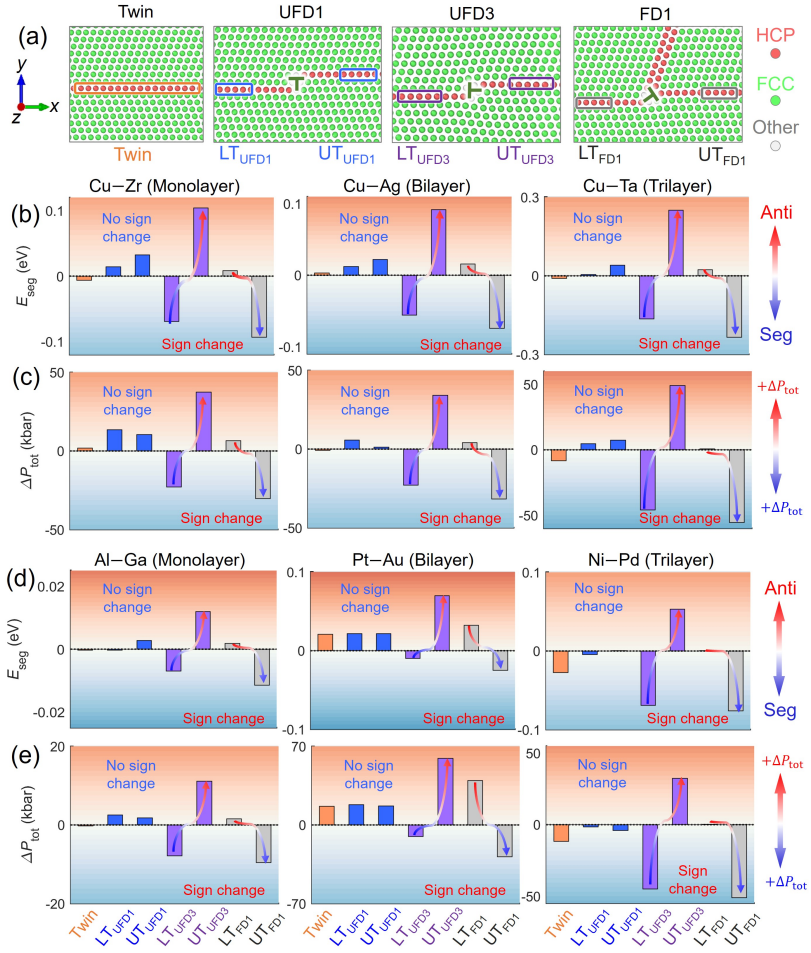

Figure 6: **Variation of the segregation energy (E_{seg}) and local pressure difference (ΔP_{tot}) of solute atoms at the boundary layer in pristine twin and unfaulted/faulted disconnections**. (a) Six different locations are chosen to calculate the average E_{seg} and ΔP_{tot} at two unfaulted disconnections, UFD1 and UFD3, and a faulted disconnection, FD1. Note that UFD3 and FD1 have the same Burgers vectors $\mathbf{b} = 1/3[1\bar{1}1]$ rotated 90° with respect to the boundary plane, while UFD1 has a Burgers vector $\mathbf{b} = 1/6[121]$ parallel to the boundary plane. The lower terrace and upper terrace regions in each disconnection are respectively denoted as LT and UT. (b) and (c) show averaged E_{seg} and ΔP_{tot} at twin and six other locations at disconnections for three Cu-based binary alloys with different segregation patterns. (d) and (e) show averaged E_{seg} and ΔP_{tot} at twin and six other locations at disconnections for three representative binary alloys with different segregation structures (single-, bi-, and multi-layer segregation patterns).

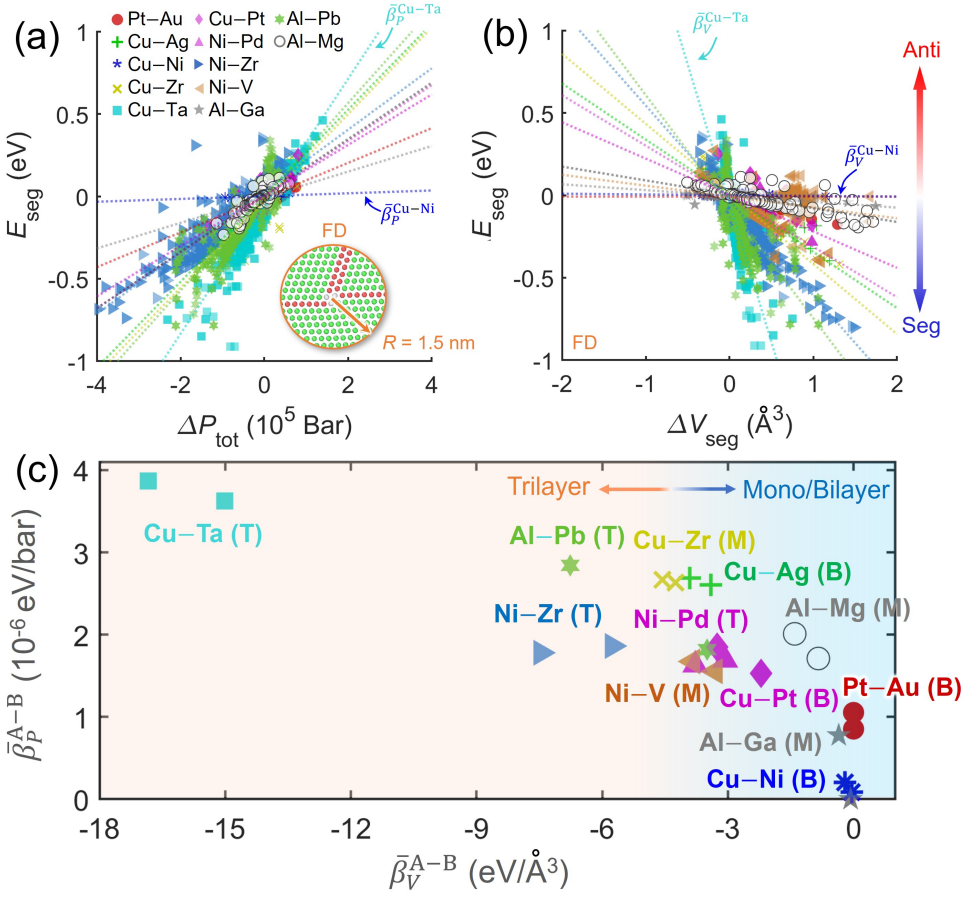

Figure 7: **Correlation analysis of segregation energy (E_{seg}) with twin-boundary descriptors for twelve binary alloy systems**. (a) Scatter plot of E_{seg} *v.s.* local pressure change (ΔP_{tot}) at faulted disconnections. All data points are extracted from a circular region near the disconnection with a cutoff radius R = 1.5 nm, see insert. The regression line of E_{seg} *v.s.* ΔP_{tot} for each binary alloy is plotted as a dotted line and the corresponding slope of each regression line ($\tilde{\beta}_{\mathrm{P}}^{\mathrm{A-B}}$, where A is the matrix element and B is solute atom) is also calculated. (b) Scatter plot of E_{seg} *v.s.* segregation volume (ΔV_{seg}) at faulted disconnections. The slope of each regression line for E_{seg} *v.s.* ΔV_{seg} curves is denoted as $\tilde{\beta}_{\mathrm{V}}^{\mathrm{A-B}}$. Similar scatter plots for unfaulted disconnection are displayed in Suppl. Fig. S16 in the Supplementary Material. (c) Scatter plot of fitted $\tilde{\beta}_{\mathrm{P}}^{\mathrm{A-B}}$ *v.s.* $\tilde{\beta}_{\mathrm{V}}^{\mathrm{A-B}}$ for both faulted and unfaulted disconnections for all twelve A–B alloys.

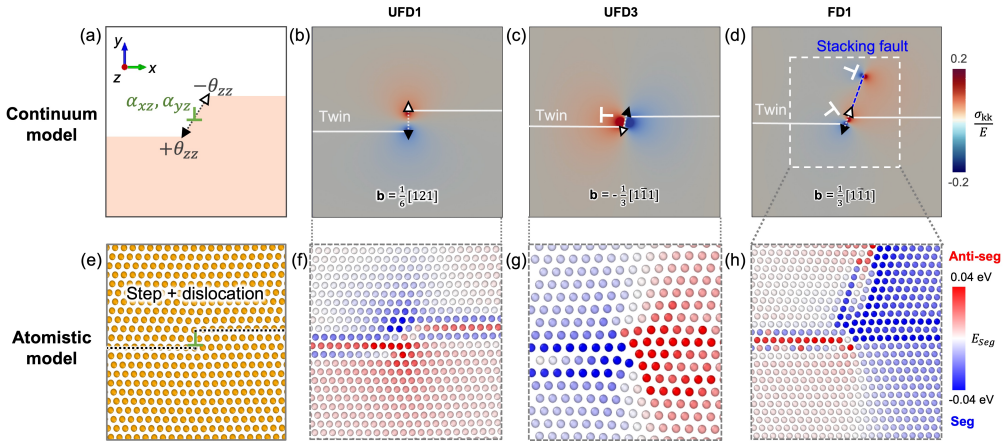

Figure 8: **Comparison of normalized hydrostatic pressure distribution vs. segregation maps for three representative disconnections**. (a) Disclination dipole construct with a positive disclination density component ($+\theta_{zz}$, black triangle symbol) at the lower terrace and a negative disclination density component ($-\theta_{zz}$, white triangle symbol) at the higher terrace [60] with Frank's vector magnitude ω. α_{xz} and α_{yz} are disclination density tensors defined by projections of the Burgers vector onto the x and y axes, respectively. The normalized hydrostatic pressure profiles for (b) UFD1, (c) UFD3, and (d) FD1 disconnections are simulated by FFT-based dislocation-disclination continuum mechanics modeling. Note that for UFD1 and UFD3 the pixel resolution is 512×512 pixels, while for FD1 the resolution is 1024×1024 pixels. (e) Atomistic model of disconnection structure optimized by molecular dynamic (MD) simulations. The MD-computed segregation energy, E_{seg}, maps of Pt–Au alloy for (f) UFD1, (g) UFD3, and (h) FD1 disconnections.

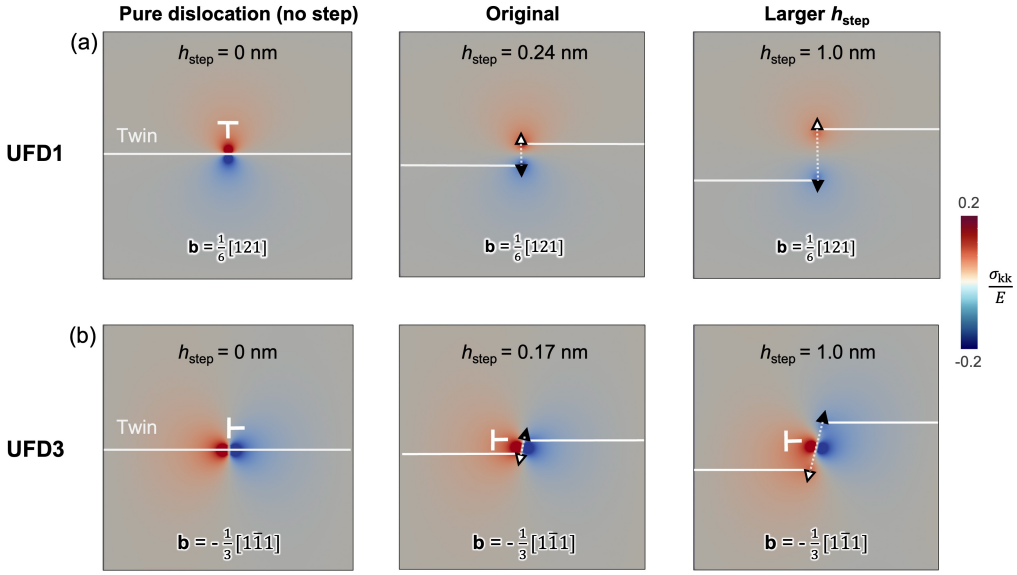

Figure 9: **Effects of the disconnection step height on the local stress field for unfaulted disconnections for hypothetical configurations**. Panel (a) shows the comparison of the normalized hydrostatic pressure profiles for between no step with only a pure dislocation (left), the original configuration, *i.e.* based on the atomistic configuration (middle), and for a configuration with a larger step height (right). Panel (b) shows the same type of comparison but for the UFD3 configurations.

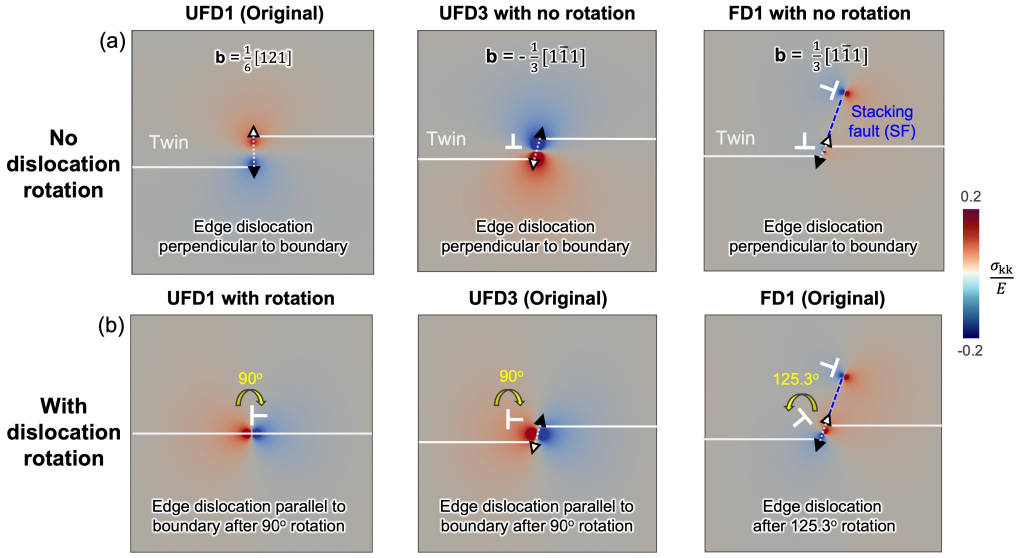

Figure 10: **Effects of rotating the orientation of dislocation's Burgers vector on the local stress field in unfaulted disconnections for hypothetical configurations**. Panel (a) shows various disconnection configurations with no dislocation rotation at the step for UFD1 (left, original configuration), UFD3 (middle, hypothetical configuration), and FD1 (right, hypothetical configuration). Panel (b) shows various disconnection configurations with the dislocation being rotated at the step for UFD1 (left, hypothetical configuration), UFD3 (middle, original configuration), and FD1 (right, original configuration). Note that for UFD1 and UFD3 the pixel resolution is 512×512 pixels, while for FD1 the resolution is 1024×1024 pixels.

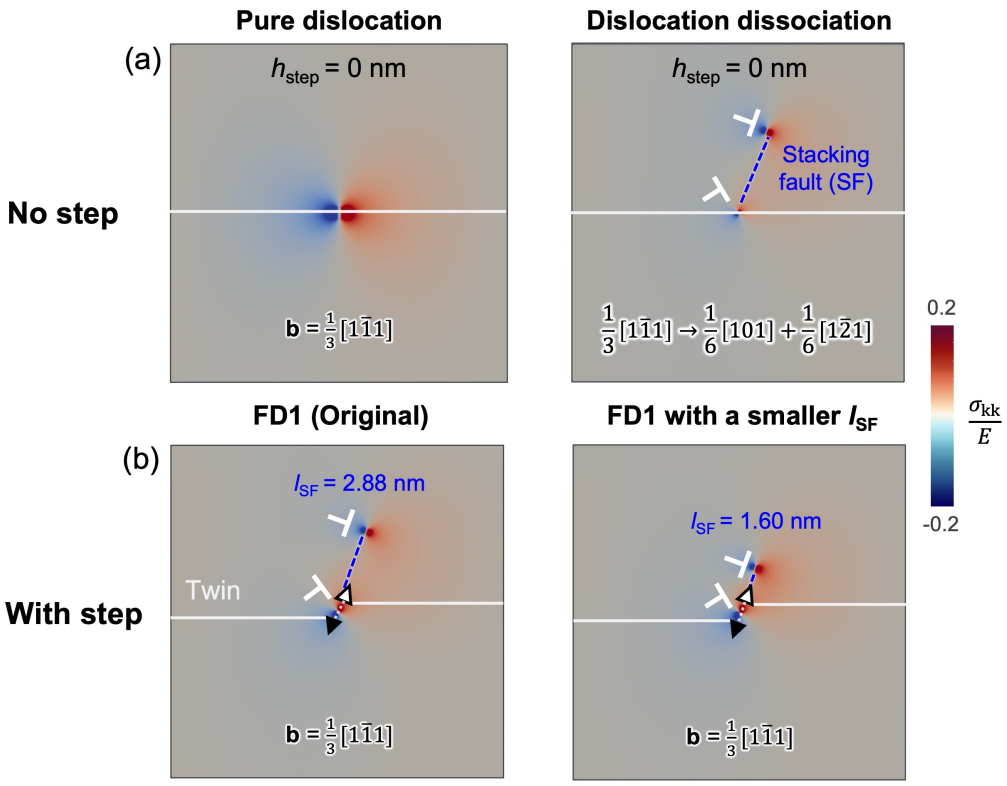

Figure 11: **Effects of disconnection step and stacking fault on the local stress field in faulted disconnection FD1 for hypothetical configurations**. Panel (a) shows two disconnection configurations with no step present for a pure dislocation configuration (left, hypothetical configuration) and a dissociated configuration with a dislocation at the boundary and a trailing stacking fault in the bulk upper crystal (right, hypothetical configuration). Panel (b) shows two disconnection configurations with a step present for FD1 (left, original configuration) and FD1 with the trailing stacking fault being closer to the step (right, hypothetical configuration).